MIKES Metrology
In collaboration with Low Temperature Laboratory, TKK
Espoo, Finland, 2009

TUNNEL JUNCTION DEVICES FOR QUANTUM METROLOGY

Antti Kemppinen

Dissertation for the degree of Doctor of Science in Technology to be presented with due permission of the Faculty of Information and Natural Sciences, for public examination and debate in Auditorium AS1 at Helsinki University of Technology (Espoo, Finland) on the 16th of October, 2009, at 12 noon.

MIKES
Centre for Metrology and Accreditation
P.O. Box 9
FI-02151 Espoo, Finland
URL: http://www.mikes.fi/
Tel. +358 10 605 4411
Antti.Kemppinen@mikes.fi

MIKES publications
ISSN 1235-2704
ISSN 1797-9730 (PDF)
J3/2009:
Antti Kemppinen: *Tunnel junction devices for quantum metrology*
Doctoral dissertation
Opponent: Prof. Per Delsing
Supervisor: Prof. Matti Kaivola
Instructor: Prof. Jukka Pekola
Keywords: *quantum metrology, tunnel junctions, single-electron transistor, superconductivity, electronic refrigeration*
ISBN 978-952-5610-53-6
ISBN 978-952-5610-54-3 (PDF)
URL: http://lib.tkk.fi/Diss/2009/isbn9789525610543/

Multiprint Oy
Espoo 2009

Abstract

This Thesis studies opportunities to create a quantum standard for the electric current with the help of tunnel junctions. We use two types of tunnel junctions: superconducting Josephson junctions, and NIS junctions where one of the electrodes is normal (N) and the other one superconducting (S). In both cases, tunnel junctions are employed in a single-electron transistor (SET) structure, which is used to transfer a controlled number k of electrons (e) with the repetition frequency f. The magnitude of the resulting current is thus $I = kef$.

First, we study the Cooper pair sluice, where Josephson junctions are connected as two superconducting quantum interference devices (SQUID). A gate electrode is used to control the charge state of the superconducting island formed between the SQUIDs. The sluice is based on tuning the tunneling rates through the SQUIDs with local magnetic fluxes, which allows to control the direction of the charge transfer. Weak traces of current quantization can be observed up to above 1 nA, which is large enough current for many metrological purposes. However, the accuracy of the current is still far from what is required in metrology. We study also a new type of SQUID structure, the balanced SQUID, which could be used to improve the accuracy of the sluice or in, e.g., some quantum computing applications.

Second, we employ NIS junctions in the hybrid (SINIS) single-electron transistor with superconducting leads and a normal-metal island. This structure can be used as the SINIS turnstile which lets electrons to flow one by one in the direction determined by the bias voltage. We report the first experimental results on the SINIS turnstile and two methods to improve the accuracy of the current: increasing the charging energy of the island or connecting the turnstile in a resistive environment. We also show that the SINIS turnstile can be used as an electronic radio-frequency refrigerator where tunneling processes cool the electron temperature of the normal-metal island.

Tiivistelmä

Tässä väitöskirjassa tutkitaan mahdollisuuksia tuottaa kvanttimekaaninen mittanormaali sähkövirralle tunneliliitosten avulla. Työssä käytetään kahden tyyppisiä tunneliliitoksia: suprajohtavia Josephson-liitoksia sekä NIS-liitoksia, joissa toinen elektrodi on normaali- (N) ja toinen suprajohtava (S). Molemmissa tapauksissa tunneliliitoksista on tehty Coulombin saartoon perustuva yhden elektronin transistorirakenne, jota käytetään siirtämään elektroneja tunnettu määrä k kerrallaan. Näin tuotettu sähkövirta on suuruudeltaan $I = kef$, missä e alkeisvaraus ja f siirron toistotaajuus, joka voidaan lukita tarkasti atomikelloihin.

Josephson-liitoksiin perustuvista rakenteista tutkitaan niin sanottua Cooperin parien sulkua. Siinä Josephson-liitoksista on tehty kaksi suprajohtavaa kvanttiinterferenssilaitetta (SQUID). Niiden väliin jäävän suprajohtavan saarekkeen varaustilaa kontrolloidaan kapasitiivisesti hilaelektrodilla. Cooperin parien sulku perustuu SQUID-rakenteiden tunneloitumisnopeuksien säätämiseen paikallisella magneettikentällä, minkä ansiosta sähkövirran suuntaa voidaan kontrolloida. Cooperin parien sululla tuotetussa virrassa voidaan havaita kvantittumista 1 nA:iin saakka, mikä on riittävän suuri moniin metrologisiin tarkoituksiin, mutta virran tarkkuus jää toistaiseksi kauas toivotusta. Työssä tutkitaan myös uudentyyppistä balansoitua SQUID-rakennetta, jota voitaisiin käyttää paitsi Cooperin parien sulun tarkkuuden parantamiseen, myös esimerkiksi kvanttilaskentasovelluksiin.

NIS-liitoksista on tässä työssä rakennettu SINIS-tyyppinen yhden elektronin transistori, jossa suprajohtavien linjojen väliin jää normaalijohtava saareke. Tätä rakennetta voidaan käyttää niin sanottuna SINIS-porttina, jossa elektroneja päästetään yksi kerrallaan jännitteen määräämään suuntaan. Väitöskirjassa esitetään paitsi ensimmäiset SINIS-portilla tehdyt kokeet, myös kaksi mahdollisuutta parantaa virran tarkkuutta joko lisäämällä transistorin varautumisenergiaa tai kytkemällä SINIS-portti resistiiviseen ympäristöön. Työssä osoitetaan myös, että SINIS-transistoria voidaan käyttää sähköisenä radiotaajuisena jäähdyttimenä, jossa tunneloitumisprosessit laskevat normaalijohtavan saarekkeen elektronilämpötilan alle kryostaatin lämpötilan.

Preface

Throughout my Thesis project, it has always been complex to describe where I work. As an employee of MIKES (Centre for Metrology and Accreditation), I was able to do the research work in the Low Temperature Laboratory of TKK (Helsinki University of Technology). This flexible arrangement was permitted by the joint quantum metrological triangle project between MIKES, TKK, and VTT Technical Research Centre of Finland.

First of all, I would like to thank my instructor, Prof. Jukka Pekola from TKK. Few graduate students get as competent and exhaustive guidance as I did. I am also grateful to Dr. Antti Manninen, my boss from MIKES, for arranging the opportunity to work on this challenging project. He has supported me in many ways from the very beginning when I started in the field of quantum electric metrology as an undergraduate student in 2003. My supervisor Prof. Matti Kaivola has helped me especially at the final bureaucratic steps of the project.

The lively working athmosphere in the PICO group of Low Temperature Laboratory makes me grateful to all the members of that group and in particular to my coauthors Dr. Sergey Kafanov, Dr. Matthias Meschke, Dr. Mikko Möttönen, Mr. Joonas Peltonen, and Dr. Juha Vartiainen. Also the people in the Electricity group at MIKES have assisted me whenever needed.

The success of our research has relied on international collaboration. The work of "the lithography wizard" Dr. Yuri Pashkin and Dr. Jaw-Shen Tsai from NEC in Japan, and the idea of resistive environment by Dr. Sergey Lotkhov and Dr. Alexander Zorin from PTB in Germany have been of great importance on the experimental side. I would also like to acknowledge the theory support of Prof. Dmitri Averin from Stony Brook University in the United States.

This Thesis would not have been possible without financial support from the Finnish Academy of Science and Letters, Vilho, Yrjö, and Kalle Väisälä Foundation. The research work has also been funded by the Academy of Finland, the Technology Industries of Finland Centennial foundation, and the European Union through the project REUNIAM.

Luckily there is life beyond physics (oh yes, there is!) and that is what has kept me going, especially during the first less productive years of the project. Therefore, I would like to acknowledge those folks relating to that part of my life.

Espoo, September 2009

Antti Kemppinen

List of publications

This Thesis consists of an overview and the following publications:

I J. J. Vartiainen, M. Möttönen, J. P. Pekola, and A. Kemppinen, *Nanoampere pumping of Cooper pairs*, Applied Physics Letters **90**, 082102 (2007).

II A. Kemppinen, A. J. Manninen, M. Möttönen, J. J. Vartiainen, J. T. Peltonen, and J. P. Pekola, *Suppression of the critical current of a balanced superconducting quantum interference device*, Applied Physics Letters **92**, 052110 (2008).

III A. Kemppinen, M. Meschke, M. Möttönen, D. V. Averin, and J. P. Pekola, *Quantized current of a hybrid single-electron transistor with superconducting leads and a normal-metal island*, in Quantum metrology and Fundamental constants, edited by F. Piquemal and B. Jeckelmann, European Physical Journal Special Topics **172**, 311–321 (2009).

IV A. Kemppinen, S. Kafanov, Yu. A. Pashkin, J. S. Tsai, D. V. Averin, and J. P. Pekola, *Experimental investigation of hybrid single-electron turnstiles with high charging energy*, Applied Physics Letters **94**, 172108 (2009).

V S. Kafanov, A. Kemppinen, Yu. A. Pashkin, M. Meschke, J. S. Tsai, and J. P. Pekola, *Single-electronic radio-frequency refrigerator*, Physical Review Letters **103**, 120801 (2009).

VI S. V. Lotkhov, A. Kemppinen, S. Kafanov, J. P. Pekola, and A. B. Zorin, *Pumping properties of the hybrid single-electron transistor in dissipative environment*, Applied Physics Letters **95**, 112507 (2009).

In Publication **I**, the author assisted in sample fabrication and measurements. In Publication **II**, the author had the main responsibility for all parts of the work from sample fabrication to experiments, simulations, and writing the paper. In Publication **III**, the author did more than half of the sample fabrication and measurements, and had the main responsibility for writing the paper. In Publication **IV**, the author did about a half of the measurements and had the main responsibility for data analysis, simulations, and writing the paper. In Publication **V**, the author participated in the measurements and did most of the data analysis and simulations. In Publication **VI**, the author did a part of the experiments and data analysis, and participated actively in writing the paper.

Contents

Chapter 1

Introduction

The globalization of trade necessitated an international agreement of a common system of measurements already in the 19th century. The Meter Convention in 1875 developed to the International System of Units, SI, in 1960 [1]. The definitions of the units were originally based on artefacts like the prototypes of the meter and the kilogram. However, already in 1870 it was pointed out [2] and later adopted as a general goal of metrology that the system of units should be based on physical phenomena and fundamental constants [3]. Such a system would have better reproducibility: unlike artefacts, the fundamental constants and the laws of physics are not expected to change. Moreover, references of the units could be realized independently from any other realizations. However, after more than hundred years of revolutions in science and engineering, an important part of the SI system is still based on an artefact, namely the prototype of the kilogram.

The development of a voltage standard based on the Josephson effect [4] in 1960's and a resistance standard based on the quantum Hall effect [5] in 1980's introduced a new concept, quantum metrology, as a promising way to realize units. The main advantage arises from the intrinsic property of quantum physics, namely the tendency that the observable quantities are quantized. Often the quantized levels can be expressed as simple formulas containing integers and fundamental constants. In addition to the practical use in metrology, the quantum standards can provide information on the laws of physics behind the standards with unrivaled precision.

Two decades ago, new ideas for manipulating single electrons with tunnel junctions [6, 7] raised hope in developing a quantum standard for the SI base unit ampere, too. Besides the use as a current standard, single electronics could provide a consistency check for the quantum standards of voltage and resistance via the quantum metrological triangle [8].

Since the 1990's, the development of the quantum current standard has focused on single-electron transistor (SET) devices [9, 10]. The relative uncertainty of about 10^{-8}, which is low enough for metrological needs, was reached finally with a SET pump formed by an array of seven tunnel junctions, but only at picoampere level [11]. The current was sufficiently high for a quantum capacitance standard [12], but not for a practical current standard nor for closing the quantum metrological triangle. The quest for higher currents has involved several candidate devices, see, e.g., Ref. [13] for a review. However, none of them has reached metrological accuracy.

This Thesis focuses on two types of single-electron devices: a superconducting pump called Cooper pair sluice [14] (Publications I–II), and a hybrid turnstile [15] consisting of both superconducting and normal-state elements (Publications III–VI).

Chapter 2

Ampere in the SI system

" *The ampere is that constant current which, if maintained in two straight parallel conductors of infinite length, of negligible circular cross-section, and placed 1 metre apart in vacuum, would produce between these conductors a force equal to* 2×10^{-7} *newton per metre of length*" [1].

The present definition of the ampere has several problems. First, the definition is not practical since the experiments required for realizations of electrical units are beyond the resources of most of the national metrology institutes. Second, the best uncertainty levels are not better than few parts in 10^{-7}, see, e.g., Ref. [16]. Third, the definition involves the unit of newton, $\mathrm{kg} \times \mathrm{m/s^2}$. Although the definitions of the second and the meter are based on constants of Nature, the electrical units are subordinate to the last of the prototype definitions, namely the mass of the kilogram.

For practical purposes, the quantum standards of voltage and resistance based on the elementary charge e and the Planck constant h have been used as *representations* of the units. The Josephson voltage standard driven at frequency f_J generates quantized voltages

$$V_\mathrm{JVS} = n_\mathrm{J} f_\mathrm{J} / K_\mathrm{J}, \tag{2.1}$$

where n_J is an integer voltage step index. The Josephson constant is

$$K_\mathrm{J} = \frac{2e}{h}(1 + \epsilon_\mathrm{J}), \tag{2.2}$$

where ϵ_J represents a possible error compared to the theoretical value $2e/h$. Correspondingly, the resistance of a quantum Hall standard can be written as

$$R_\mathrm{QHR} = R_\mathrm{K} / i_\mathrm{K}, \tag{2.3}$$

where i_{K} is the step index. The von Klitzing constant is

$$R_{\mathrm{K}} = \frac{h}{e^2}(1 + \epsilon_{\mathrm{K}}). \tag{2.4}$$

Since 1990, there is an international agreement for the values of the Josephson and von Klitzing constants to be used for metrological purposes: $K_{\mathrm{J}-90} = 483597.9$ GHz/V and $R_{\mathrm{K}-90} = 25812.807\ \Omega$ [1]. Despite the agreement, the present status of electrical metrology is unacceptable, since electrical metrologists are working outside the SI system.

There are two main competitors for a new method to realize the kilogram: the Watt balance experiment [17, 18] and the Avogadro project [19]. The first would trace the kilogram from the electrical units, and the latter from a known number of silicon atoms. Although there is currently a mismatch between the two methods, Mills *et al.* have proposed that new definitions of units based on fundamental constants should be adopted to the SI system by the 24th General Conference on Weights and Measures (CGPM) in 2011 [20]. Since the proposal, there has been plenty of discussion on whether and how to change the system [21–23].

In the new SI system, the ampere would be defined in terms of the transport of elementary charges. The current would be written as

$$I_{\mathrm{SET}} = k_{\mathrm{S}} Q_{\mathrm{S}} f_{\mathrm{S}}. \tag{2.5}$$

Here, an integer number k_{S} of charges

$$Q_{\mathrm{S}} = e(1 + \epsilon_{\mathrm{S}}) \tag{2.6}$$

are transported with frequency f_{S}. There are two potential error types: transfering incorrect number of charges, and a deviation from the assumption $Q_{\mathrm{S}} = e$. The first could be tested with an electrometer [11]. The latter requires comparison to other experiments, e.g., vie the quantum metrological triangle proposed originally in Ref. [8], see Refs. [13, 24] for recent reviews.

The quantum metrological triangle is illustrated in Fig. 2.1. The triangle experiment employs Ohm's law $V = RI$ for a comparison between the quantum standards of voltage, resistance and current. By substituting Eqs. (2.1), (2.3), and (2.5) to Ohm's law, the result equation of the triangle becomes

$$\frac{n_{\mathrm{J}} i_{\mathrm{K}}}{2k_{\mathrm{S}}} \frac{f_{\mathrm{J}}}{f_{\mathrm{S}}} = 1 + \epsilon_{\mathrm{J}} + \epsilon_{\mathrm{K}} + \epsilon_{\mathrm{S}}. \tag{2.7}$$

The outcome of the triangle experiment is thus the sum of the error terms. In principle it is possible that these error terms would compensate each other, but in practice this is very unlikely.

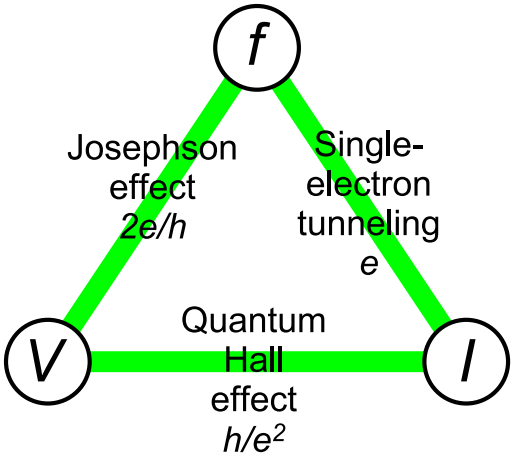

Figure 2.1: The quantum metrological triangle.

Reference [24] discusses the interpretation of a hypotetical result of the triangle experiment. The best estimates for the error terms deduced from other experiments are presently $\epsilon_{\mathrm{K}} = (0.2 \pm 0.18) \times 10^{-7}$, $\epsilon_{\mathrm{J}} = (2.38 \pm 7.20) \times 10^{-7}$ and $\epsilon_{\mathrm{S}} = (-1.0 \pm 9.2) \times 10^{-7}$. Hence the triangle has to be closed with a relative uncertainty of about 10^{-8} to yield new information about ϵ_{K}, but an experiment in the 10^{-7} range would be significant for the other legs of the triangle.

As argued in Ref. [24], both theoretical and experimental knowledge on the assumption $Q_{\mathrm{S}} = e$ is weak. The present estimate for ϵ_{S} is based on a single experiment, namely the indirect triangle experiment at NIST [12, 25]. In that experiment, the 7-junction SET pump was used to transfer a known amount of charge to a capacitor with capacitance C traceable to the calculable capacitor [26]. The voltage over the capacitor was compared to the Josephson voltage. The relation $Q = CV$ was thus used instead of Ohm's law. Regardless of the lack of knowledge on Q_{S}, the definition of the ampere is based on transfering single electrons in the proposal for the new SI system, Ref. [20]. Hence, another measurement of ϵ_{S} would be crucial for metrology. A potential setup for the direct closure of the triangle already exists at LNE in France, but there are still some irreproducibilities on the level of 10^{-4} [27]. In Finland, there is also an ongoing project to build a triangle setup in collaboration between MIKES, TKK, and VTT.

Besides the devices studied in this Thesis, there are also several other candidates for generating the quantized current of about 100 pA or more that would allow the direct closure of the quantum metrological triangle. Implementing on-chip resistors in series with the SET pump allows to reduce the number of

junctions to three [28]. The current of 16 pA with the statistical relative error of 3.9×10^{-6} was demonstrated recently [29]. Several scientifically interesting superconducting devices have been proposed or tried [30–32], but they are still far from metrological accuracy. Semiconducting structures can be used to pump electrons with the help of surface-acoustic waves [33] or a tunable potential in a GaAs nanowire [34–36] or in a Si nanowire MOSFET [37, 38]. The semiconducting devices can generate currents up to the nanoampere range, but the relative uncertainties have been limited to about the 10^{-4} range to date. Still another interesting possibility is to improve the accuracy by measuring the current transport with the precision of single electrons [39, 40].

Chapter 3

Tunnel junctions

A tunnel junction consists of an insulating layer between two conducting electrodes. The insulating layer must be very thin so that the wavefunctions of electrons in the electrodes can overlap. Electrons can then be transfered through the junction by quantum mechanical tunneling.

The properties of a tunnel junction depend strongly on the electrodes. Metallic tunnel junctions can be divided into three categories: NIN, NIS and SIS junctions (N = normal-metal, I = insulator and S = superconductor). The latter belongs also to Josephson junctions in which tunneling can carry supercurrent [4]. The first single-electron pumps were based on NIN junctions [10, 11]. This Thesis discusses the opportunities of Josephson junctions and NIS junctions for quantized current transport.

3.1 Coulomb blockade and the single-electron transistor

The electrostatic energy of a capacitor is $Q^2/2C$. The energy required to charge a capacitor with a single electron, the *charging energy*, is thus $E_\mathrm{c} = e^2/2C$. It gives the energy scale for the single-electron effects which can be significant if the capacitance is small. More specifically, the manipulation of single electrons is feasible if the charging energy is much larger than the energy scale of thermal fluctuations, i.e., $E_\mathrm{c} \gg k_\mathrm{B}T$. Here, k_B and T are the Boltzmann constant and temperature, respectively. The charging energy is often expressed in the unit of temperature, e.g., $E_\mathrm{c}/k_\mathrm{B} \approx 0.9$ K when $C = 1$ fF. Thus the operation of single-electron devices requires low temperatures. Manipulating single electrons by ultrasmall tunnel junctions was proposed in the 1980's [6, 8]. Such junctions are attractive for electrical metrology because their capacitances can be in the range

where the charging energy is important, and because the electrons usually tunnel one by one. See, e.g., Refs. [7, 41–44] for reviews on single-electron transport in tunnel junctions.

The single-electron transistor (SET) is a structure with two tunnel junctions and a *gate electrode* connected to a conducting island, see Fig. 3.1(a). The total capacitance of the island is $C_\Sigma = C_0 + C_\mathrm{r} + C_\mathrm{l} + C_\mathrm{g}$, where C_0 is the self-capacitance, and r, l and g refer to the right and left tunnel junctions and to the gate, respectively. The charging energy of the island is thus

$$E_\mathrm{c} = \frac{e^2}{2C_\Sigma}. \tag{3.1}$$

At zero bias ($V_\mathrm{l} = V_\mathrm{r} = 0$), the electrostatic energy of the SET in the charge state with n extra electrons on the island is

$$E_\mathrm{ch} = E_\mathrm{c}(n - n_\mathrm{g})^2, \tag{3.2}$$

where $n_\mathrm{g} = V_\mathrm{g}C_\mathrm{g}/e$ is the normalized gate charge. The parabolic dependence of E_ch on n_g is illustrated in Fig. 3.1(b) for several charge states.

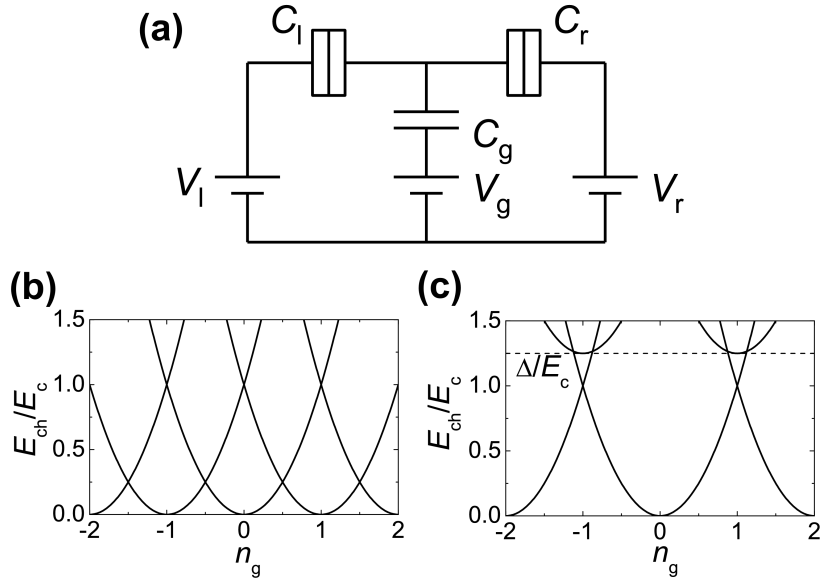

Figure 3.1: (a) Schematic of the single electron transistor. (b) Electrostatic energies of the charge states in a SET as a function of the gate charge. Here, the island is normal metal. (c) Electrostatic energies of the SET with a superconducting island. The energies of the charge states with odd n are lifted by the BCS gap Δ.

In the sequential tunneling model, which first was described in Ref. [6] and which is also often called the orthodox model, electrons are assumed to tunnel one by one. Since any single-electron tunneling event changes the charge state of the island, at least two states are required for current transport through the SET. At the degeneracy points of the SET, i.e., when n_g is a half integer, two states share the minimum energy and current transport is possible with any nonzero bias voltage. At integer values of n_g, the energy of magnitude E_c has to be supplied to change the charge state. This effect is called the Coulomb blockade.

The electrostatic energy change in tunneling through the junction i to (+) or from (−) the island can be expressed as

$$E_n^{i,\pm} = \pm 2E_\mathrm{c}(n - n_\mathrm{g} \pm 1/2) \pm e(V_i - \nu) \tag{3.3}$$

where n is the initial charge state and $\nu = (C_\mathrm{l}V_\mathrm{l} + C_\mathrm{r}V_\mathrm{r})/C_\Sigma$ is the offset to the island potential from the single junctions. Often one omits the offset ν by assuming symmetric junctions, $C_\mathrm{l} = C_\mathrm{r}$, and symmetric bias, $V_\mathrm{l} = -V_\mathrm{r} \equiv V/2$. At integer values of n_g, the energy required to change the charge state from the minimum can then be supplied by applying the bias voltage $eV = 2E_\mathrm{c}$.

In the limit of a perfect voltage bias, the leads relax to the equilibrium state quickly after each tunneling event. Then the Fermi Golden Rule approximation gives simple expressions for the single-electron tunneling rates:

$$\begin{aligned} \Gamma_n^{i,+} &= \tfrac{1}{e^2 R_{\mathrm{T},i}} \textstyle\int_{-\infty}^{\infty} dE f(E, T_\mathrm{lead})[1 - f(E - E_n^{i,+}, T_\mathrm{island})] \\ \Gamma_n^{i,-} &= \tfrac{1}{e^2 R_{\mathrm{T},i}} \textstyle\int_{-\infty}^{\infty} dE f(E + E_n^{i,-}, T_\mathrm{island})[1 - f(E, T_\mathrm{lead})]. \end{aligned} \tag{3.4}$$

Here, $f(E, T)$ is the Fermi function, and T_lead and T_island are the temperature of the leads and the island, respectively. The tunneling rates are proportional to the number of occupied states to tunnel from and to the number of free states to tunnel to. The density of states is assumed to be constant close to the Fermi energy. The properties of the electrodes and the tunnel barrier are described with a single parameter, the tunneling resistance $R_{\mathrm{T},i}$, which can be determined experimentally. At low temperatures, the electron–phonon coupling is weak, and hence the electronic temperature of the leads and especially that of the small-volume island can differ from the bath temperature. The electron–electron coupling is usually strong enough to maintain the Fermi distribution [45].

At finite temperatures, the charge state of the island can be described by the probability distribution P_n. In the steady state, the distribution is constant and the net probability of transition between adjacent states is zero. Hence, the master equation gives the steady state

$$[\Gamma_n^{\mathrm{l},+} + \Gamma_n^{\mathrm{r},+}]P_n = [\Gamma_{n+1}^{\mathrm{l},-} + \Gamma_{n+1}^{\mathrm{r},-}]P_{n+1}. \tag{3.5}$$

The current through junction l is simply

$$I_{\rm l} = -e \sum_{n=-\infty}^{\infty} P_n[\Gamma_n^{\rm l,+} - \Gamma_n^{\rm l,-}]. \tag{3.6}$$

In the steady state $I_{\rm l} = I_{\rm r}$.

Simulated current–voltage (IV) curves of a SET at low temperature $k_{\rm B}T \approx E_{\rm c}/20$ are presented in Fig. 3.2. In the gate-closed state ($n_{\rm g}$ is an integer), the current vanishes in the voltage range $|eV| < 2E_{\rm c}$. In the gate-open state ($n_{\rm g}$ is half-integer), there is a resistive slope at all voltages, but at low voltages, the resistance is doubled. This is because there are only two allowed charge states. After an electron has been added to the island, an electron must tunnel away before the next entry is possible.

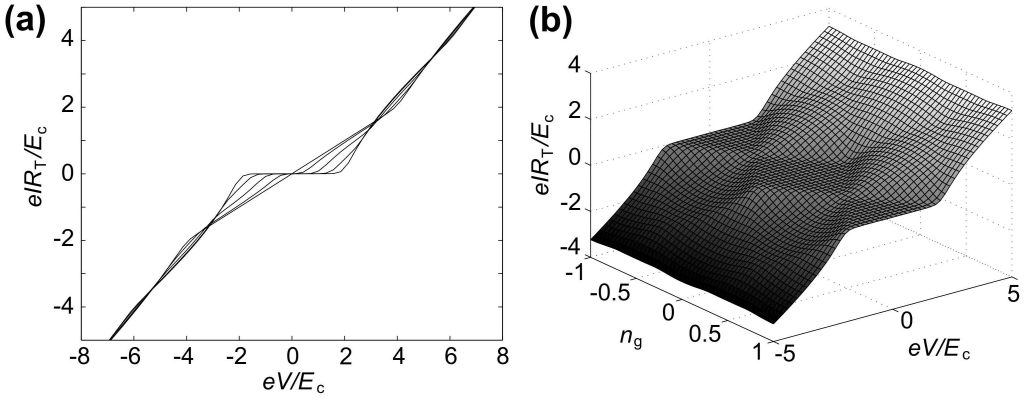

Figure 3.2: (a) Simulated dc IV curves of a SET at different gate values. (b) Current of a SET as a function of V and $n_{\rm g}$. In the flat regions, called Coulomb diamonds, single n states are stable, and the current through the device is ideally zero [III].

In superconductors, charge carriers are either Cooper pairs or quasiparticles (unpaired electrons). In an ideal superconductor, there are no quasiparticle states in the BCS energy gap Δ [46]. Hence the electrons tend to be paired, and energies of the odd charge states of a SET with a superconducting island are lifted by Δ. This is illustrated in Fig. 3.1(c). In the case $\Delta > E_{\rm c}$, the minimum energy state has an even number of electrons on the island at all gate charge values. Ideally, this should result into a $2e$ periodic behaviour of the SET. In practice, nonequilibrium quasiparticles often destroy the $2e$ periodicity that is crucial for many potential applications of superconducting SETs. The physics of the nonequilibrium quasiparticles is still somewhat unclear, although several recipes for obtaining $2e$ periodicity have been reported [47–52].

3.2 Josephson junctions

A Josephson junction is a weak link between two superconducting electrodes [4]. The link is such a thin layer of non-superconducting material that a supercurrent can flow through the junction. In this Thesis, we consider only SIS junctions where the supercurrent is carried by the tunneling of Cooper pairs. Properties of Josephson junctions are reviewed, e.g., in Refs. [46, 53, 54].

3.2.1 Josephson effects

According to the Ginzburg–Landau theory, superconductivity can be described by the macroscopic wavefunction $\psi(\vec{r}) = \sqrt{n_\mathrm{s}} e^{i\theta(\vec{r})}$, where n_s is the density of Cooper pairs and $\theta(\vec{r})$ is the phase of the wavefunction. One can often assume that the phase is spatially constant in the small electrodes of a Josephson junction. The supercurrent through the junction is then given by the *dc Josephson relation*

$$I_\mathrm{s} = I_\mathrm{c} \sin\phi, \tag{3.7}$$

where $\phi \equiv \theta_1 - \theta_2$ is the phase difference between the electrodes. The critical current, i.e., the maximum supercurrent that can flow in the junction, is given by the Ambegaokar-Baratoff formula [55]

$$I_\mathrm{c} = \frac{\pi\Delta}{2eR_\mathrm{T}} \tanh\left(\frac{\Delta}{2k_\mathrm{B}T}\right). \tag{3.8}$$

The *ac Josephson relation* describes the increment of the phase difference under a dc voltage:

$$\frac{d\phi}{dt} = \frac{2e}{\hbar} V. \tag{3.9}$$

From Eqs. (3.7) and (3.9) one can derive the energy of the supercurrent, i.e., the work done by a current source to change the phase difference, $\int I_\mathrm{s} V dt = -E_\mathrm{J} \cos\phi$, where $E_\mathrm{J} = \hbar I_\mathrm{c}/2e$ is called the Josephson coupling energy. The total current through a Josephson junction can be described by the resistively and capacitively shunted junction (RCSJ) model, see Fig. 3.3(a), where the supercurrent element is shunted with capacitance C and resistance R. The total current can be written as

$$I = \frac{\hbar C}{2e}\ddot{\phi} + \frac{\hbar}{2eR}\dot{\phi} + I_\mathrm{c}\sin\phi. \tag{3.10}$$

The dynamics of the Josephson junction can be understood with the help of the following mechanical analog. A particle with the mass $(\hbar/2e)^2 C$ is moving along the ϕ axis in the *tilted washboard potential*

$$U(\phi) = -E_\mathrm{J}\left(\frac{I}{I_\mathrm{c}}\phi + \cos\phi\right), \tag{3.11}$$

which is illustrated in Fig. 3.3(b). Dissipation of the system can be described with the viscous drag force $(\hbar/2e)^2\dot{\phi}/R$. Since our focus is on single-electron effects, we consider small junctions with low capacitance (mass) and critical current and with relatively high resistance (low damping). The dynamics is thus typically the following, see Fig. 3.3(c). At small current bias, the particle is localized within a potential well and the voltage ($V \propto d\phi/dt$) is zero. When the current is increased, there is a finite probability that the particle escapes the well by thermal activation or by macroscopic quantum tunneling. After the escape, the particle starts flowing along the potential, the mean velocity being that corresponding to the voltage $eV = 2\Delta$. When the bias current is lowered again, the particle is retrapped to a well only below the retrapping current $I_\mathrm{r} \ll I_\mathrm{c}$. The junction is thus hysteretic. In the presence of damping, the particle can localize to the next well causing only a voltage spike. This phenomenon, called phase diffusion, is seen as a small dc voltage, averaged from the spikes by the measurement circuitry. In very small junctions, damping in the superconducting state can be stronger than in the normal state. Phase diffusion is then possible also with hysteretic (low I_r) junctions. This phenomenon is called underdamped phase diffusion [56–59].

As shown in Fig. 3.3(c), the escape to the normal state can happen well below I_c. Moreover, this is a statistical process. Often it is more reliable to probe the superconducting properties in the escape measurement where current pulses of constant length are sent to the junction. Increasing the magnitude of the current pulse increases the probability of switching to the normal state which can be recorded as a voltage pulse. The resulting switching histogram, i.e., probability of the escape as a function of the magnitude of the current pulse, is a useful way to measure the electric current or the quantum mechanical properties of several kinds of systems, see, e.g., Refs. [56, 57, 60, 61].

An important application of small Josephson junctions is the superconducting single-electron transistor (SSET). For Cooper pairs, Eq. (3.3) is rewritten as

$$E_{n,2e}^{i,\pm} = \pm 2E_{\mathrm{c},2e}(n_{2e} - n_{\mathrm{g},2e} \pm 1/2) \pm 2e(V_i - \nu), \tag{3.12}$$

where $E_{\mathrm{c},2e} = (2e)^2/2C_\Sigma$ and n_{2e} are the charging energy and the excess number of Cooper pairs, respectively. The gate charge normalized for Cooper pairs is $n_{\mathrm{g},2e} = C_\mathrm{g}V_\mathrm{g}/2e$. Often the SSET can be treated as a coherent quantum system where the charge on the island and the phase difference over the SSET are conjugate variables obeying the Heisenberg uncertainty principle [46]. Hence, systems of small Josephson junctions can also be used as building blocks of quantum bits [62, 63].

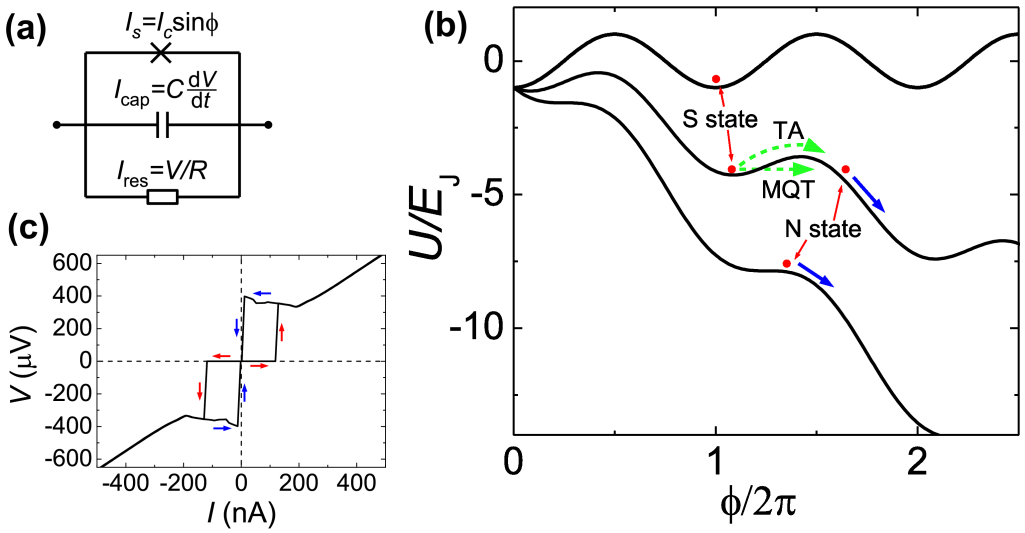

Figure 3.3: (a) Components of current transport in the RCSJ model. (b) Washboard potentials for currents $I = 0, I_c/2, I_c$. In the superconducting (S) state, the system is localized in one of the potential wells. At $I = I_c$, the well vanishes, but the particle can escape the well already at $I < I_c$ due to either thermal activation (TA) over the barrier or macroscopic quantum tunneling (MQT) through the barrier. In most cases, escape leads to transition to the normal (N) state, i.e., the particle starts flowing freely in the tilted potential. In the presence of damping, the escaped particle can be localized in the next well and this phase slip causes just a voltage spike. (c) A typical measured hysteretic IV curve of a Josephson junction. Equation (3.8) gives the value $I_c \approx 270$ nA for the critical current. When the current is being increased, the junction jumps to the normal state before reaching the critical current (red arrows). When the current is lowered, the conservation of kinetic energy keeps the particle in the N state. Only at the retrapping current, damping can localize the particle in the S state (blue arrows).

3.2.2 Critical current of the dc SQUID

The dc SQUID is a circuit with two Josephson junctions in a loop, see Fig. 3.4(a). The supercurrent through the SQUID can be expressed simply as $I_{SQ} = I_{c1}\sin\phi_1 + I_{c2}\sin\phi_2$, where $I_{c,i}$ and ϕ_i are the critical current and the phase difference of the junction i, respectively. The magnetic flux of the loop, Φ_{tot}, sets a constraint on the phase differences:

$$\phi_1 - \phi_2 = 2\pi\frac{\Phi_{tot}}{\Phi_0} \pmod{2\pi}, \tag{3.13}$$

where $\Phi_0 = h/2e \approx 2.07 \times 10^{-15}$ Vs is the magnetic flux quantum. The magnetic flux is the sum of the external flux Φ_{ext} and the fluxes induced by the currents

in the loop:

$$\Phi_{\rm tot} = \Phi_{\rm ext} + L_1 I_{\rm c1} \sin\phi_1 - L_2 I_{\rm c2} \sin\phi_2. \tag{3.14}$$

Here, L_i are the loop inductances, see Fig. 3.4(a).

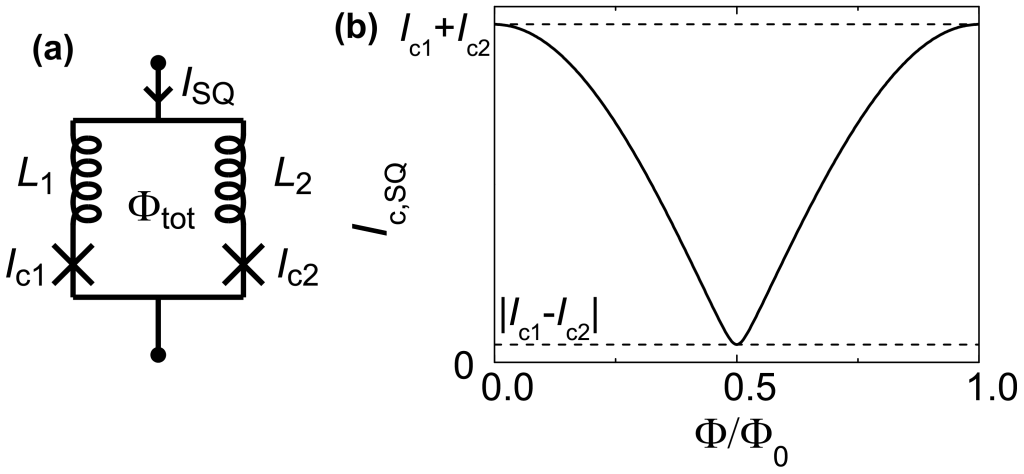

Figure 3.4: (a) Schematic of the dc SQUID. (b) Critical current of the dc SQUID as a function of the magnetic flux. Here, the inductances are negligible, and $I_{\rm c2} = 0.9 I_{\rm c1}$.

The effect of the loop inductance can be neglected in the limit $2\pi L_i I_{{\rm c},i}/\Phi_0 \ll 1$. Since we are interested in small junctions, this is usually the case. Then an analytic formula can be derived for the critical current of the SQUID. The current of the SQUID is now $I_{\rm SQ} = I_{\rm c1} \sin\phi_1 + I_{\rm c2} \sin(\phi_1 + \vartheta)$, where $\vartheta = 2\pi\Phi_{\rm ext}/\Phi_0$. Maximizing this current with respect to ϕ_1, the critical current of the SQUID becomes

$$I_{\rm c,SQ} = \sqrt{I_{\rm c1}^2 + I_{\rm c2}^2 + 2 I_{\rm c1} I_{\rm c2} \cos\vartheta}. \tag{3.15}$$

The magnetic flux can thus be used to tune the critical current of the dc SQUID in the range $|I_{\rm c1} \pm I_{\rm c2}|$, see Fig. 3.4(b). In the case $I_{\rm c1} = I_{\rm c2}$, the critical current is simply $I_{\rm c,SQ} = 2 I_{\rm c1} |\cos(\vartheta/2)|$. The critical current can thus ideally be tuned to zero by setting $\Phi_{\rm ext} = 0.5\Phi_0$. However, any difference in the critical currents of the junctions or any inductance in the SQUID loop causes a residual critical current $I_{\rm res}$. In the limit $I_{\rm c1} \gg I_{\rm c2}$, the modulation becomes sinusoidal: $I_{\rm c,SQ} \approx I_{\rm c1} + I_{\rm c2} \cos\vartheta$. There is a variety of applications for the dc SQUID. In this Thesis, we employ it as a tunable Josephson element in the manner suggested, e.g., in Refs. [62, 63].

3.3 NIS junctions and the hybrid single-electron transistor

Typical applications of NIS junctions are microcoolers [64–66] and thermometers [67–69], both reviewed in Ref. [70]. In these applications, NIS junctions are usually employed in the double-junction (SINIS) geometry. The opposite NISIN geometry has gathered less attention and is also less relevant for this Thesis. Recently, there has been interest in SINIS structures with considerable charging energy. They have been proposed for single-electron cooler applications [71, 72] that are closely related to the quantized current application [15] studied in this Thesis. Also thermometry in the Coulomb-blockaded case has been considered [73].

The dominating current transport mechanism in a NIS junction is single-electron tunneling between the normal metal and the quasiparticle states of the superconductor. The main difference compared to NIN junctions is the BCS quasiparticle density of states $n_{\mathrm{S}}(E) = |E/\sqrt{E^2 - \Delta^2}|$. Hence there are ideally no states in the BCS gap $|E| < \Delta$.

Let us first consider the double junction (SINIS) geometry with negligible charging energy. The effect of the BCS gap can be explained qualitatively with the band diagram of Fig. 3.5. Voltage V over the structure shifts the Fermi levels of the superconductors by $\pm eV/2$. At low temperatures, the Fermi distribution is almost like a step function. Due to energy conservation, electrons can tunnel only horizontally. At low voltages, electrons cannot tunnel from the occupied states of the normal metal to the superconductors, where the corresponding energy levels are either forbidden or occupied. Similarly, there are no empty states in the normal metal at the occupied energy range of the superconductors. Therefore, the BCS gap Δ causes a voltage range $-2\Delta < eV < 2\Delta$ where the current through the device is very small. The effect of the BCS gap on the IV curve is thus qualitatively similar to that of the Coulomb blockade in Fig. 3.2.

In Fig. 3.5(b), the structure is biased close to the edge of the gap. Electrons can tunnel from the left superconductor to the states slightly below the Fermi energy of the normal metal filling cold states, whereas hot electrons above the Fermi level of the normal metal can tunnel to the quasiparticle states of the right superconductor. The electron–electron interactions usually maintain the Fermi distribution [45], but it narrows which means that the normal metal cools down.

The charge current of a hybrid (SINIS) single-electron transistor can be described similarly as that of the normal-state transistor in Sec. 3.1, except that the BCS density of states has to be introduced to the tunneling rates of Eq. (3.4):

$$\begin{aligned} \Gamma_n^{i,+} &= \tfrac{1}{e^2 R_{\mathrm{T},i}} \textstyle\int_{-\infty}^{\infty} dE n_{\mathrm{S}}(E) f_{\mathrm{S}}(E)[1 - f_{\mathrm{N}}(E - E_n^{i,+})], \\ \Gamma_n^{i,-} &= \tfrac{1}{e^2 R_{\mathrm{T},i}} \textstyle\int_{-\infty}^{\infty} dE n_{\mathrm{S}}(E) f_{\mathrm{N}}(E + E_n^{i,-})[1 - f_{\mathrm{S}}(E)]. \end{aligned} \tag{3.16}$$

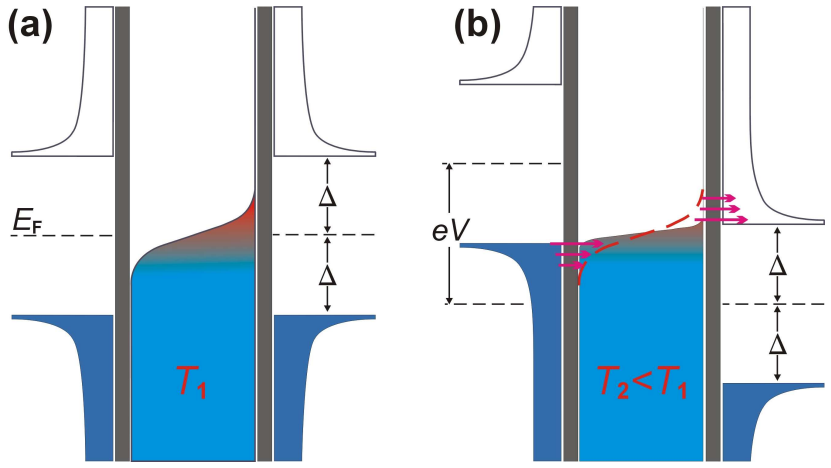

Figure 3.5: Schematic band diagram of the SINIS structure biased with (a) a zero voltage and (b) the voltage V across the structure. For the superconducting leads, we show the BCS density of states which is zero in the range $E_F \pm \Delta$, where E_F is the Fermi level and Δ is the BCS energy gap. Close to the edges of the gap, the density of states approaches infinity. The states below the gap are almost perfectly occupied, and those above the gap are empty. In the normal metal, the Fermi function describing the occupancy of the states is shown instead of the density of states, which is roughly constant within the narrow energy range presented here. For these illustrations, the gap has been narrowed for clarity. Applying voltage across the sample shifts the Fermi levels of the superconductors by $\pm eV/2$. In (b), eV is slightly below 2Δ, and the normal metal cools down. In the formulas in the text we set the reference level of energy as $E_F = 0$ [III].

Here, f_N and f_S refer to the Fermi functions at the temperature of the normal-metal island and that of the superconducting leads, T_N and T_S, respectively. The latter we try to thermalize to the bath temperature, but the temperature of the island can vary significantly.

Simulated current-voltage (IV) curves of a hybrid SET are presented in Figs. 3.6(a–b), compare to Fig. 3.2. The current is negligible within the BCS gap also in the gate-open state. The Coulomb diamonds are extended by the gap and the stability regions of the neighboring charge states overlap.

In the measurements of both NIS and SINIS samples, a small leakage current in the sub-gap region is practically always observed. Typically, the leakage current is linear at low voltages, which is demonstrated in Fig. 3.6(c). The leakage is often

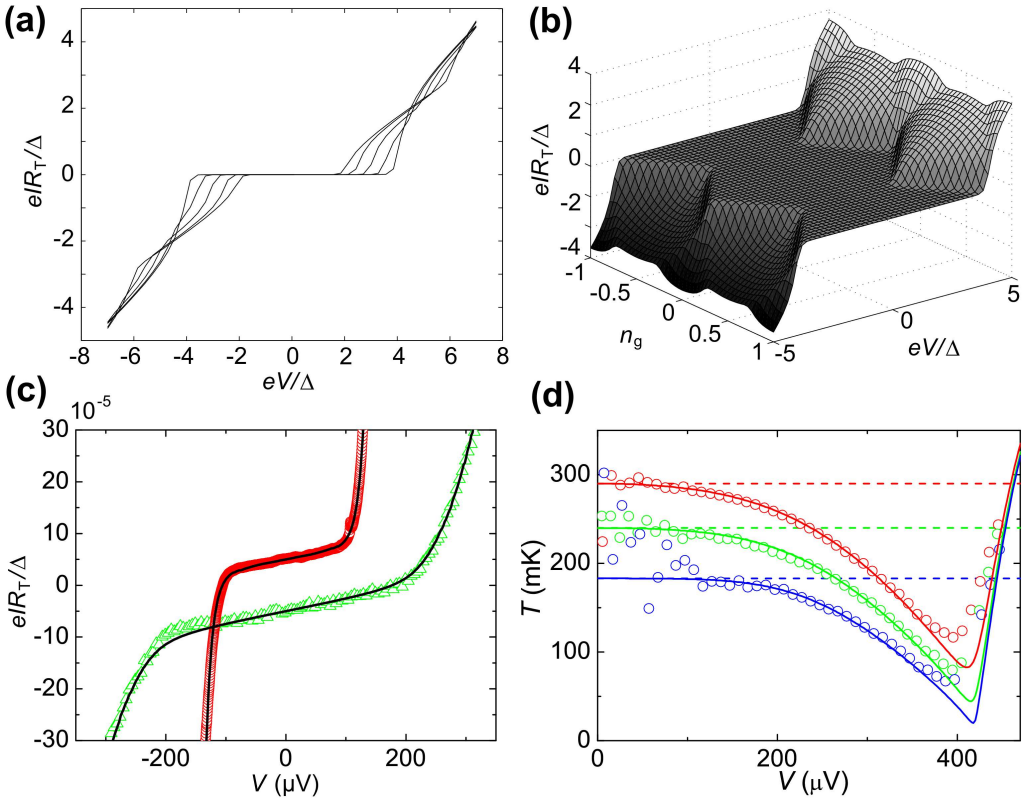

Figure 3.6: (a) Simulated dc IV curves of a hybrid SET at different gate values. The current is blockaded by the BCS gap at voltages $|eV| < 2\Delta$ even in the gate-open state. (b) Current of a hybrid SET as a function of V and n_g. The Coulomb diamonds are extended by the BCS gap. The neighboring diamonds overlap close to the half-integer values of n_g. (c) Normalized sub-gap currents of a single NIS junction with $R_T = 60.5$ kΩ (red circles) and the SINIS transistor sample B of Publication IV in the gate-open state (green triangles). The normalized currents were shifted by $\pm 5 \times 10^{-5}$ for clarity. The slopes of the linear regions correspond to $\eta = 4.5 \times 10^{-5}$ and $\eta = 4.7 \times 10^{-5}$ for the NIS and the SINIS sample, respectively. The black lines are simulated IV curves with parameters $\gamma = 4.5 \times 10^{-5}$ and $T_S = 115$ mK for the NIS sample and $\gamma = 9.4 \times 10^{-5}$ and $T_S = 120$ mK for the SINIS sample. (d) Simulated temperature of the island in the SINIS transistor sample B in the gate-open (solid lines) and gate-closed (dashed lines) states at bath temperatures 183 mK (blue), 240 mK (green) and 290 mK (red). The circles show the corresponding experimentally extracted temperatures. Figs. (a-b) reproduced from [III].

described by introducing a smeared density of states [74]

$$n_S(E) = \left| \mathrm{Re} \frac{E + i\Gamma}{\sqrt{(E + i\Gamma)^2 - \Delta^2}} \right|. \tag{3.17}$$

The smearing parameter Γ can be conveniently written in the normalized form $\gamma = \Gamma/\Delta$, which gets typically a value of $\gamma \approx 10^{-4}$ in junctions with Al as the superconductor [70]. The smeared density of states yields the finite resistance of the linear region $R_0 = R_\mathrm{T}/\gamma$ around zero bias in NIS samples and also in the SINIS case if the charging energy is negligible. In the hybrid single-electron transistor, leakage is suppressed in the gate-closed state. In the gate-open state, the resistance is doubled as in Fig. 3.2: $R_0 = 2R_\mathrm{T}/\gamma$. To avoid confusion, we typically refer to the leakage as the ratio $\eta = R_\mathrm{T}/R_0$. The smeared density of states (3.17) was originally proposed to take into account the Cooper pair breaking and quasiparticle lifetime effects at the gap edge [75], but there is no proof that this would be the physical origin of the sub-gap leakage. Hence, Eq. (3.17) should be considered as a phenomenological model. This leakage issue is crucial for many of the applications of NIS junctions, and it is discussed in detail in Sec. 6.3.

The heat fluxes arising from tunneling are proportional to the energy deposition and extraction rates of incoming and outgoing electrons:

$$\begin{aligned} \dot{Q}_n^{i,+} &= \tfrac{1}{e^2 R_{\mathrm{T},i}} \textstyle\int_{-\infty}^{\infty} dE (E - E_n^{i,+}) n_\mathrm{S}(E) f_\mathrm{S}(E) [1 - f_\mathrm{N}(E - E_n^{i,+})] \\ \dot{Q}_n^{i,-} &= \tfrac{1}{e^2 R_{\mathrm{T},i}} \textstyle\int_{-\infty}^{\infty} dE (E + E_n^{i,-}) n_\mathrm{S}(E) f_\mathrm{N}(E + E_n^{i,-}) [1 - f_\mathrm{S}(E)]. \end{aligned} \tag{3.18}$$

The total heat current to the island due to tunneling is

$$\dot{Q}_\mathrm{t} = \sum_{n=-\infty}^{\infty} P_n [\dot{Q}_n^{\mathrm{l},+} + \dot{Q}_n^{\mathrm{r},+} - \dot{Q}_n^{\mathrm{l},-} - \dot{Q}_n^{\mathrm{r},-}], \tag{3.19}$$

where the probability distribution P_n is calculated from the tunneling rates (3.16) and the steady-state equation (3.5). The temperature of the island is set by the heat balance between tunneling and the electron–phonon coupling

$$\dot{Q}_\mathrm{e-ph} = \Sigma \mathcal{V} (T_\mathrm{bath}^5 - T_\mathrm{N}^5), \tag{3.20}$$

where $\mathcal{V}$, T_bath and Σ are the volume of the island, temperature of the phonon bath, and the electron–phonon coupling constant, respectively. The electron–phonon coupling constant depends on the material, e.g., $\Sigma \approx 2 \times 10^9$ W/m^{3}K^5 for copper [70]. The equilibrium temperature is found iteratively by searching for the balance $\dot{Q}_\mathrm{t} + \dot{Q}_\mathrm{e-ph} = 0$.

Examples of the island temperature as a function of the bias voltage are presented in Fig. 3.6(d). This sample was used in Publications IV (sample B) and V. There can be significant cooling close to the BCS gap, as expected based on Fig. 3.5. The cooling effect can be controlled by the gate. Hence the device acts as a heat transistor [72]. In this simulation, the island volume was very small, only about $30 \times 50 \times 80$ nm^3, and the model predicts very low island temperatures.

In practice, tunneling induces quasiparticles into the superconductors which can be heated locally close to the junctions [76–78]. Quasiparticle backscattering then smears the cooling effect which is observed in the experimentally extracted temperature (for details of the temperature extraction method, see Sec. 6.5). However, the simple model described above is sufficient for the Thesis, since it is valid except at the gap edges.

3.4 Effects beyond the basic tunneling theory

The ideal picture given above for single-electron tunneling is satisfactory in many cases. In this Section, the most relevant deviations to the ideal model are introduced. They can be divided in two classes:

First, the energy of the system was assumed to be conserved in all tunneling events. However, the quantum mechanical system is not isolated. There can be energy exchange between the studied system and its dissipative electromagnetic environment.

Second, we assumed that tunneling is sequential, i.e., electrons or Cooper pairs tunnel one by one according to the Fermi Golden Rule approximation. However, there are higher order processes, i.e., correlated transfer of several particles.

3.4.1 Coupling to the electromagnetic environment

The effect of the electromagnetic environment on the single-electron tunneling rates is discussed thoroughly, e.g., in Ref. [42]. The dissipative environment is formulated as a set of harmonic oscillators [79]. Based on the Fermi Golden Rule, the tunneling rates can be described with the $P(E)$ function formalism, where P is the probability to emit ($E > 0$) the energy E to the external circuit, or to absorb it ($E < 0$). The tunneling rates of, e.g., Eq. (3.16) now become

$$\begin{aligned}\Gamma_n^{i,+} &= \tfrac{1}{e^2 R_{\mathrm{T},i}} \int_{-\infty}^{\infty} dE \int_{-\infty}^{\infty} dE' n_{\mathrm{S}}(E) f_{\mathrm{S}}(E)[1 - f_{\mathrm{N}}(E')]P(E - E' - E_n^{i,+}) \\ \Gamma_n^{i,-} &= \tfrac{1}{e^2 R_{\mathrm{T},i}} \int_{-\infty}^{\infty} dE \int_{-\infty}^{\infty} dE' n_{\mathrm{S}}(E') f_{\mathrm{N}}(E)[1 - f_{\mathrm{S}}(E')]P(E - E' - E_n^{i,-}).\end{aligned} \tag{3.21}$$

In the case of a single junction, the impedance seen by the junction is given by the external impedance $Z(\omega)$ and the capacitive reactance of the junction itself in parallel: $Z_{\mathrm{t}} = (i\omega C + Z^{-1}(\omega))^{-1}$. The same equation is valid for the SET (double junction) case, but C is replaced by the capacitance of the two junctions in series, $C_{\mathrm{eff}} = C_{\mathrm{l}} C_{\mathrm{r}}/(C_{\mathrm{l}} + C_{\mathrm{r}})$. In addition, the other junction suppresses the effect of the electromagnetic environment on junction i by the factor $\kappa_i^2 = (C_{\mathrm{eff}}/C_i)^2$. For example, in the case of a single junction, $\kappa_i = 1$, and in the case of identical junctions ($C_{\mathrm{l}} = C_{\mathrm{r}}$), $\kappa_i = 1/2$.

The energy exchange probability

$$P(E) = \frac{1}{2\pi\hbar}\int_{-\infty}^{\infty} dt \exp[\kappa_i^2 J(t) + \frac{i}{\hbar}Et] \tag{3.22}$$

is the Fourier transform of the phase–phase correlation function

$$J(t) = 2\int_0^{\infty} \frac{d\omega}{\omega}\frac{\mathrm{Re}Z_\mathrm{t}(\omega)}{R_\mathrm{K}}\left\{\coth\left(\frac{\hbar\omega}{2k_\mathrm{B}T}\right)[\cos(\omega t)-1] - i\sin(\omega t)\right\}. \tag{3.23}$$

Here, $R_\mathrm{K} = h/e^2$ is the resistance quantum.

Except for a few special cases, $P(E)$ function has to be calculated numerically [42]. In the limit $Z(\omega) = 0$, $P(E) = \delta(E)$, which reproduces the tunneling rates of Sec. 3.1. In the limit $Z(\omega) = R \gg R_\mathrm{K}$, one finds that

$$P(E) = \frac{1}{\sqrt{4\pi\kappa_i^2 E_\mathrm{c} k_\mathrm{B}T}} \exp\left[-\frac{(E-\kappa_i^2 E_\mathrm{c})^2}{4\kappa_i^2 E_\mathrm{c} k_\mathrm{B}T}\right], \tag{3.24}$$

This result can be further simplified in the limit of low temperature $k_\mathrm{B}T \ll E_\mathrm{c}$: $P(E) = \delta(E - \kappa_i^2 E_\mathrm{c})$. The high-ohmic environment thus results in an additional charging energy which is present even in the case of a single junction. This phenomenon is sometimes called dynamical Coulomb blockade.

The $P(E)$ method can also be applied for Josephson junctions. In contrast to the quasiparticle states, Cooper pairs exist only at the chemical potential. The integration over energies can thus be neglected, and Eq. (3.21) simplifies to the form

$$\Gamma_{n,2e}^{i,\pm}(V) = \frac{\pi}{2\hbar}E_\mathrm{J}^2 P(E_{n,2e}^{i,\pm}), \tag{3.25}$$

see the electrostatic energy change of Eq. (3.12). In addition, the resistance quantum R_K in Eq. (3.23) is replaced by the resistance quantum of Cooper pairs, $R_\mathrm{Q} = h/4e^2$. However, since the Josephson coupling was taken into account as a perturbation, this treatment is valid only in the case

$$E_\mathrm{J} P(E_{n,2e}^{i,\pm}) \ll 1. \tag{3.26}$$

The effect of the electromagnetic environment on small Josephson junctions turns out to be a very complicated problem [80]. One reason is that it is essential to know the impedance of the environment up to frequencies in the upper gigahertz range. At the highest frequencies, the impedance is typically of the order of the vacuum impedance $\sqrt{\mu_0/\epsilon_0} \approx 377\ \Omega$, regardless of if the junction is voltage or current biased at dc. In general, current-biased junctions behave hysteretically as in Fig. 3.3, but the measured maximum supercurrent is well below

the critical current and depends strongly on noise and the high-frequency environment [57]. At low-ohmic bias, the supercurrent peak of perfect zero-voltage bias is transformed into a peak at low voltages [80]. In addition, peaks in $Z(\omega)$ at resonance frequencies ω_r result in current peaks at voltages $\hbar\omega_\mathrm{r}/2e$ in the sub-gap regime [81]. Although the $P(E)$ theory is often valid for the resonance peaks, the higher supercurrent peak can be estimated only when $E_\mathrm{J} \ll E_\mathrm{c}$ [42]. In this case, the maximum supercurrent is proportional to I_c^2, as can be seen from Eq. (3.25). In the regime $E_\mathrm{J} \leq E_\mathrm{c}$, the height and the shape of the supercurrent peak has only been calculated in the case of a very carefully designed low-ohmic environment [82]. Then the junction is not hysteretic and the theory of classical phase diffusion is valid [83].

3.4.2 Higher-order processes

Higher-order processes are reviewed, e.g., in Refs. [43, 84]. The simplest higher-order process is called cotunneling, i.e., coherent transfer through two or more junctions simultaneously. Cotunneling is the dominant higher-order process in normal-state SETs and important also in superconducting SETs. It is indeed the cotunneling effect that sets the requirement for a long array of junctions in the normal-state pump [11]. Cotunneling can be suppressed by placing resistors close to the SET [28, 85].

In the SINIS transistor, cotunneling can occur only above the BCS gap [86]. In the sub-gap regime, which is the most relevant voltage range for this Thesis, the dominant higher-order process is usually Andreev reflection, where two electrons of the normal metal tunnel into a Cooper pair or vice versa. In the ballistic limit, Andreev reflection yields a linear slope at low voltages. However, when the junction size is much larger than the electron mean free paths in the metals, Andreev reflection can occur diffusively, which can yield much larger currents. Moreover, there is a conductance peak at zero voltage [87].

Charging energy can set voltage thresholds also for Andreev reflection. This issue has been studied experimentally in NISIN transistors [88, 89], but for SINIS transistors, only theoretical considerations exist [86]. Nevertheless, when Andreev reflection is Coulomb-blockaded, the dominant electron transport mechanism in SINIS transistors can be Cooper-pair–electron cotunneling, where transport over a single junction is correlated with the transport of an electron over the whole transistor in the same direction [86].

Chapter 4

Experimental methods

4.1 Sample fabrication

All the samples of the Thesis were fabricated by electron beam lithography and by using the shadow angle technique [90]. We used two common variants: the two-layer process with PMMA (polymethylmethacrylate) and copolymer (PMMA–MAA, polymethylmetacrylate–methacrylic acid) resists [91], and the three-layer process with germanium between the resists [92], see Fig. 4.1. Both processes are based on bombarding the resist layers sensitive to electrons by the tightly focused electron beam of a scanning electron microscope (SEM). The electron beam breaks the long molecule chains of the polymer resists, which makes the patterned areas soluble for a developer. We used a mixture of MIBK (methyl isobutyl ketone) and IPA (isopropanol) as the developer. After preparing the mask, the samples were metalized in an electron gun evaporator where metal lying in a small crucible is heated and evaporated by electron beam. Tunnel junctions are often based on aluminum which gets a thin uniform and insulating layer (tunnel barrier) when oxidized in $\lesssim 1$ mbar for a few minutes.

The two-layer process is simpler, which makes it useful for many purposes. However, the three-layer process has a better resolution which is important for fabricating samples with high charging energy and could also help in fabricating SQUIDs with identical junctions. The two-layer process was used in Publications I–III and the three-layer process in Publications IV–VI. For Publications IV–V, patterning was done at NEC in Japan and the evaporation in Finland. The samples of Publication VI were fabricated completely at PTB in Germany. They required evaporation in three angles: first Cr in oxygen for making on-chip CrO_x resistors, Al directly on top of that (NS contact), and finally normal metal on top of the oxidized aluminum (NIS contact).

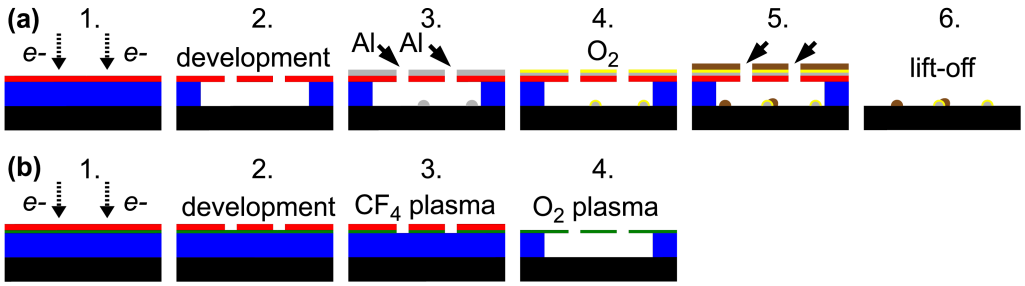

Figure 4.1: (a) Two-layer sample fabrication process. 1. About 500 nm of copolymer (blue) and 150 nm of PMMA (red) resists are spinned on oxidized silicon wafer (black). The resists are patterned with electron beam. 2. The sample is developed in MIBK/IPA 1:3 solvent and rinsed in IPA. Development dissolves the resist where polymers have been broken. The copolymer resist has a low resolution and a high sensitivity to electrons, hence a cavity is formed under the sharp PMMA pattern. 3. Aluminum (grey) is evaporated in an angle. 4. The surface of the aluminum layer is oxidized, which forms the tunnel barrier (yellow). 5. Another electrode (brown) is evaporated in an opposite angle to form a tunnel junction. 6. The rest of the resists are dissolved with acetone, which removes also the extra metal from the top. (b) Three-layer germanium process. 1. About 30 nm layer of Ge (green) is evaporated between the two resists. Patterning is done as in (a). 2. The PMMA layer is developed. 3. The pattern of the PMMA is etched to the Ge layer in CF_4 plasma. 4. The PMMA layer is removed and the cavity is formed by oxygen plasma etching. The rest of the process is the same as in (a).

4.2 Cryogenic methods

All experiments were carried out in a self-made plastic ^{3}He–^{4}He dilution refrigerator with a base temperature of about 50 mK and with a cooling power of about 40 μW at 100 mK [93]. The dilution refrigerator can effectively cool down the lattice of the sample. At low temperatures, however, the electron–phonon coupling is weak, see Eq. (3.20), and the temperature of the electron system can be significantly higher than that of the refrigerator. It is thus crucial to thermalize the wiring of the cryostat carefully.

The effect of thermal noise coming from the high-temperature parts of the measurement setup on single-electron devices has been analyzed, e.g., in Ref. [94]. Low-frequency noise can be filtered with standard RC or LC filters which, however, lose their performance in the gigahertz range due to parasitic effects. On the other hand, it is the large energy $\hbar\omega$ of the high-frequency noise photons that broaden the $P(E)$ function (3.22) most significantly.

Several self-made high-frequency filters have been reported, e.g., powder filters [95, 96] and microfabricated filters [97]. In this Thesis, we used the Thermocoax lossy coaxial lines [98]. All of these solutions can be used to reach the needed attenuation [99].

After Publication I, we designed a new sample stage with 12 Thermocoax filtered dc lines and a possibility to connect 5 rf lines. Each Thermocoax line was about 1.5 m long, of which ~ 0.5 m was between the base temperature and ~ 1 K, and ~ 1 m was wound to the base temperature. At higher temperatures, we used twisted pairs for the dc lines. The electronic heating on typical samples coming via the wiring is of the order of 1 fW [69]. Even much lower heat loads have been reported [100].

Also the high-frequency lines need to be thermalized, but since they couple to the sample only via very low capacitance or mutual inductance, no powder filtering was applied. The lines where thermalized to 4 K by standard 50 Ω attenuators. In Publications I-III, flexible thin coaxial lines were used. Their attenuation increased already at relatively low frequencies. This resulted significant heating at frequencies as low as ~ 20 MHz, when a typical control signal was passed to the sample. Hence, we shifted to semi-rigid niobium coaxial lines, which can be used up to at least 1 GHz.

4.3 Traceability of low currents

Interest to measure subnanoampere currents has increased during the past decade, driven, e.g., by radiation dosimetry and semiconductor testing. Also the development of single-electron transport devices requires both high-resolution measurements and comparison to conventional standards. A current meter with subfemtoampere resolution (Keithley 6430) is even commercially available. Hence, several national metrology institutes have developed the traceability of very low currents [101–104].

The most typical way of measuring low electrical currents is to use an operational amplifier with a feedback resistor R_f, see Fig. 4.2(a). The amplifier generates the voltage $V = R_\mathrm{f} I$ and tries to keep the voltage of the input at the virtual ground. Hence the input resistance of the meter can be relatively low. This method can be used for traceable current measurements by calibrating the feedback resistor and the voltage meter. Below 1 nA, however, the nonidealities of large resistors make this increasingly difficult [103].

Traceability of the lowest currents is usually based on the capacitor charging method, because very low-loss gas-dielectric capacitors become available in that range. A typical scheme for traceable current measurement is presented in Fig. 4.2(b). The current charges the capacitor and produces the voltage ramp

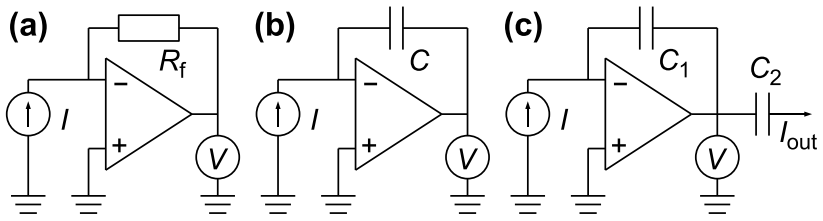

Figure 4.2: Schemes for current measurement with (a) resistive and (b) capacitive feedback. (c) Scheme for a traceable current generator based on differentiating a voltage ramp with the gas-dielectric capacitor C_2.

$dV/dt = I/C$. Lower uncertainty can usually be achieved by current generation with a related method, see Fig. 4.2(c). A voltage ramp is produced with the amplifier circuit, measured and differentiated to the current $I = C_2 dV/dt$ through the gas-dielectric capacitor C_2. In the national low-current standard of MIKES, the voltage ramp is generated with a digital-to-analog converter [104].

Our current measurements were done with DL instruments 1211 current amplifier, which is based on the circuit of Fig. 4.2(a). Agilent 34401A multimeter was used to measure the resulting voltage. For Publication IV, we considered several methods to perform traceable measurements. We tried the method of Fig. 4.2(b) along the lines of Ref. [103] employing Keithley 6517 as the operational amplifier. The problem was that the operation requires occasional decharging of the capacitor with the zero-check switch of Keithley 6517, which creates transient voltages at the input that burned our SINIS sample. Next, we tried to use Keithley 6430 current meter that was calibrated with the MIKES low-current standard. Unfortunately the relatively high input noise of the meter disturbed the operation of our sample. Finally, we used the calibrated Keithley 6430 to calibrate our usual setup based on DL 1211. The gain of DL 1211 was measured to be stable within few parts in 10^{-4} at the current sensitivities 10^{-10} A/V and 10^{-9} A/V. The main drawbacks compared to Keithley 6430 were higher measurement noise and more unstable input bias. Since the polarity of our SINIS current source can be changed easily, it was straightforward to determine the input bias in each measurement. Hence we were able to measure currents at the uncertainty of about 10^{-3} in the range of about 10 pA.

When approaching the uncertainties expected for quantum standards, the conventional ways to measure currents are no more available. At the moment, the state-of-the art of non-quantum measurements is the vibrating reed electrometer of Ref. [105] which can reach the uncertainty 1.5×10^{-5} in the picoampere range. For uncertainties below that, one can try to count the errors of the single-electron transport, see Refs. [11, 39, 40]. One possibility is to measure the current with the help of a cryogenic current comparator [29]. Also the quantum metro-

logical triangle can be considered as a precision current measurement where the traceability comes from the Josephson voltage and the quantum Hall resistance standards.

Chapter 5

Josephson junction devices

In this section, we discuss results on a Cooper pair pump, called the Cooper pair sluice (Publication I), and present a study of a new type of SQUID structure, namely the balanced SQUID (Publication II). The latter could be used to improve the accuracy of the Cooper pair sluice or, e.g., in quantum computing applications.

5.1 Cooper pair sluice

The Cooper pair sluice, proposed originally in Ref. [14], is a tunable SSET where Josephson junctions have been replaced by dc SQUIDs. The operation of the sluice is illustrated in Fig. 5.1. The critical currents of the SQUIDs are small, and the inductances of the loops can be neglected. The junctions of the SQUIDs are as identical as possible to have very low residual critical current $I_{\mathrm{c,res}} = |I_{\mathrm{c1}} - I_{\mathrm{c2}}|$. The SQUIDs can be considered here as tunable Josephson junctions, i.e., as valves that can be opened or closed for tunneling. In the beginning of the control sequence, the gate charge is set to $n_{\mathrm{g,2e}} = n_1$ and both SQUIDs are closed by applying magnetic flux. Now, one of the SQUIDs, say SQUID 1, is opened. Then the gate charge is ramped to $n_{\mathrm{g,2e}} = n_2$. The charge state of the island follows the gate charge by tunneling through SQUID 1. Next, SQUID 1 is closed again and SQUID 2 is opened. The gate charge is ramped back to n_1, and tunneling occurs now through SQUID 2. Finally, SQUID 2 is closed. This cycle transfers $n_2 - n_1$ Cooper pairs trough the island.

The Cooper pair sluice was invented to tackle the problem described in Ref. [106]. It considers Cooper pair pumping in an array of Josephson junctions in the coherent picture, where the voltage over the junction is zero and thus the phase difference over the device φ is constant. The pumping accuracy

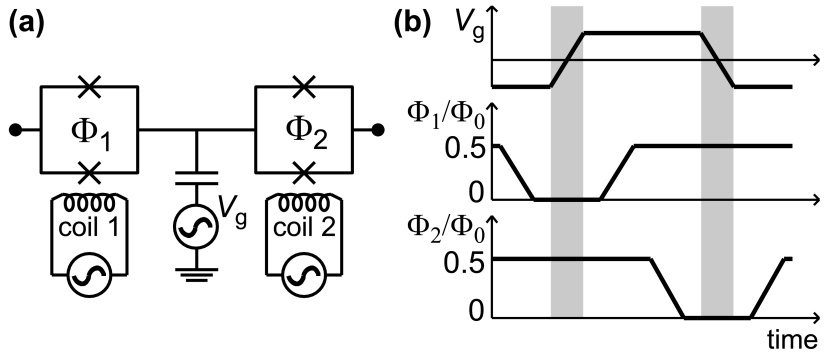

Figure 5.1: (a) Schematic of the Cooper pair sluice. It is controlled with three rf control parameters, the gate voltage V_g, and two on-chip coils that determine the magnetic fluxes Φ_i of the SQUIDs. (b) The pulse sequence used to pump Cooper pairs. Charge is being transfered in the grey time zones.

is limited by two major error sources, the supercurrent leakage which is proportional to $I_c \sin\varphi$ and the so-called coherent correction, proportional to $I_c \cos\varphi$. The latter arises from the fact that Cooper pair states are not perfectly localized, but superpositions spread over several islands. It is impossible to choose φ so that both of these errors are eliminated. In the Cooper pair sluice, these errors are proportional to $I_{c,res} \sin\varphi$ and $I_{c,res} \cos\varphi$ instead. Hence, the accuracy of the sluice depends on how well the critical currents of the SQUIDs can be suppressed, in practice how identical junctions one can fabricate. One should note, however, that the condition of a zero voltage with a constant phase can be fulfilled only for pumping in a superconducting loop [61, 107], which is not the case for a practical pump connected, e.g., to a current amplifier. On the other hand, the resulting phase fluctuations may improve the accuracy if the averages $\langle\cos\varphi\rangle$ and $\langle\sin\varphi\rangle$ vanish.

The first experimental realization of the sluice was reported in Ref. [108]. Quantization of the pumped current transport was demonstrated up to about 10 pA as a difference between the two current directions. However, the errors were of about the same order of magnitude as the pumped current due to imperfect critical current suppression.

We started trying to improve the Cooper pair sluice by studying samples with dc SQUID arrays instead of single SQUIDs. The number of control parameters was still three, since all SQUIDs on each side of the junction were operated with a single coil. This geometry helped to decrease the leakage, but pumping was not possible due to parasitic capacitances from the gate electrode to the extra islands between the SQUIDs.

In Publication I, we present improved experimental results on the Cooper

pair sluice. Upgraded sample fabrication process helped in getting more identical junctions. Long but narrow SQUID loops allowed us to reduce the cross couplings from coil 1 to SQUID 2 and vice versa. Hence, unlike in the first experiments, there was no need to apply tricky compensation pulses to keep one of the SQUIDs closed while the other one was opened. With these improvements, the leakage errors were suppressed compared with Ref. [108].

IV characteristics of the sluice when applying the pumping signals are presented in Fig. 5.2(a). Close to zero voltage, there is a leakage supercurrent peak which makes the current very sensitive to the bias voltage. However, the current is relatively constant in the sub-gap region, which indicates that the impedance of the electromagnetic environment does not have serious resonances. An optimal bias point is in a local minimum of the IV curve which minimizes both the leakage current and the bias voltage dependence of the current. We checked if the system could be modeled with the $P(E)$ theory. However, the validity criterion (3.26) is not fulfilled for the supercurrent peak, and modeling of the environment peaks is challenging. In principle, engineering the environment could help for both issues [109]. However, the relatively large SQUID loops prevent from placing components close to the junctions.

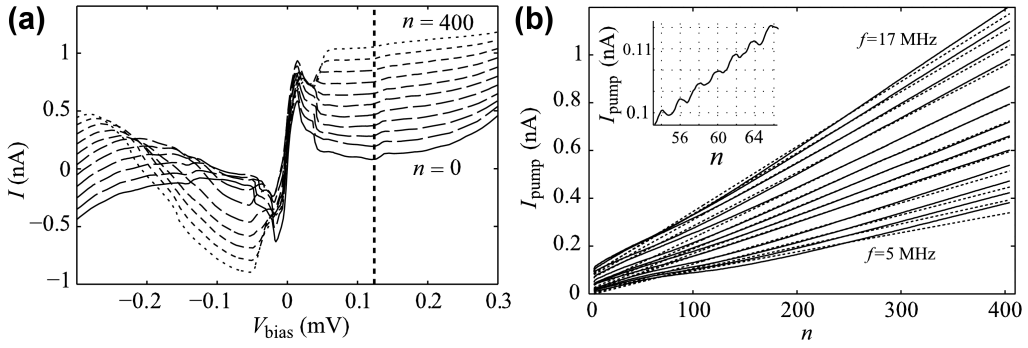

Figure 5.2: (a) IV characteristics for pumping at 15 MHz. The number of electrons pumped per cycle ranges from 0 to 400. Dashed vertical line shows the selected bias voltage. (b) Pumped current of the sluice as a function of gate amplitude for frequencies from 5 MHz to 17 MHz. The dotted theoretical currents $I = nef + I_{\mathrm{leak}}$ were forced to match the experimental current at $n = 250$, with I_{leak} as a fitting parameter. The inset shows the gate periodicity of the current [I].

The current of the sluice as a function of the number of electrons pumped per cycle is presented in Fig. 5.2(b). Leakage current of the order of tens of picoamperes remains although it was minimized by the selection of the bias voltage. The gate voltage signal was symmetric with respect to zero as shown in Fig. 5.1(b), and thus only an even number of Cooper pairs can be pumped per cycle, which

should result in $4e$ periodicity. However, the current is $2e$ periodic as shown in the inset which indicates that the experiment suffers from quasiparticle poisoning as in Ref. [108]. Despite these nonidealities, a weak trace of current quantization in the form of gate periodicity persists up to 400 electrons per cycle, and the pumped current can exceed 1 nA, which was the main achievement in this measurement.

5.2 Balanced SQUID

Already in the first proposal of the Cooper pair sluice, Ref. [14], it was suggested that the suppression of the critical current could be improved by using a more complicated SQUID structure. One of the junctions of the dc SQUID would be replaced by a small dc SQUID. This resolves the junction homogeneity issue, since the "junctions" of the big SQUID could be tuned to be identical. A similar structure has also been suggested for quantum computing applications [110–113]. In Publication II, we present the first experimental study of this structure, which we named as the balanced SQUID. A schematic of the balanced SQUID is presented in Fig. 5.3(a). For reasons explained below, we found the symmetric structure with a large middle junction and roughly identical side junctions optimal instead of the SQUID in a SQUID structure.

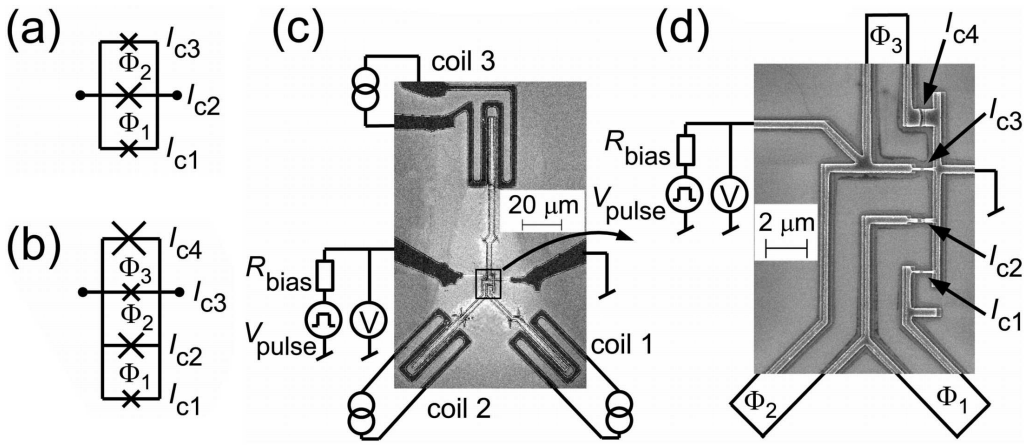

Figure 5.3: (a) Balanced SQUID. The middle junction is larger than the others. (b) Balanced SQUID and the detector junction. (c) Scanning electron micrograph of the sample showing the on-chip coils and the narrow SQUID loops, and a simplified sketch of the measurement setup. (d) Magnified view of the junctions and a sketch of the SQUID loops [II].

Since even the maximum critical current of our balanced SQUID was only of

the order of tens of nanoamperes, any direct measurement of the critical current is unreliable as discussed in Sec. 3.4.1. We solved this problem by adding a detector junction with $I_{c4} > 100$ nA in parallel with the balanced SQUID, see Fig. 5.3(b–d). This superconducting shunt protects the balanced SQUID from the electromagnetic environment. Hence we were able to employ switching histograms to measure the critical current of the whole system. The critical current of the balanced SQUID was determined from the amplitude of the sinusoidal modulation around I_{c4}. The measured critical current of the balanced SQUID is presented in Fig. 5.4(a).

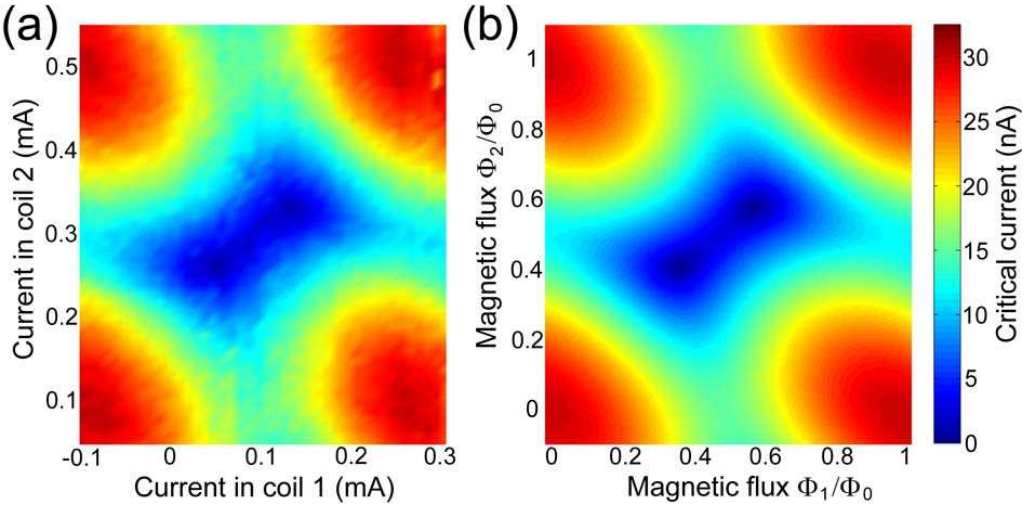

Figure 5.4: (a) Measured critical current of the balanced SQUID as a function of the coil currents. The maximum is shifted from zero current due to an offset flux. (b) Respective theoretical flux modulation of the critical current calculated with the parameters fitted from the measurement [II].

The balanced SQUID or more generally any system of n Josephson junctions in parallel forming $n-1$ loops can be modeled along the lines presented in Sec. 3.2.2. In the limit of zero inductances, the supercurrent is $I_S = I_{c1}\sin\phi_1 + I_{c2}\sin(\phi_1 - \vartheta_1) + \ldots + I_{c,n}\sin(\phi_1 - \vartheta_1 - \ldots - \vartheta_{n-1})$, where $\vartheta_i = 2\pi\Phi_{\mathrm{ext},i}/\Phi_0$ depends on the magnetic flux $\Phi_{\mathrm{ext},i}$ of loop i. The critical current of the whole structure $I_c(\vartheta_1, \ldots, \vartheta_{n-1})$ can be solved with the help of trigonometric identities. We used this analytic solution to fit the critical currents of the junctions of the sample. The theoretical flux modulation of the balanced SQUID based on these parameters is presented in Fig. 5.4(b).

The benefits of the symmetric design can be seen from the flux modulation charts of Fig. 5.4. The flux modulation of the SQUID is periodic in the square where Φ_1 and Φ_2 are between 0 and Φ_0. The critical current has the maximum

value at the corners of the square. When the critical current of the SQUID is tunable to zero ($I_{c2} \leq I_{c1} + I_{c3}$), there are two minimum points in the middle region of the chart close to the line $(0,0) \rightarrow (\Phi_0, \Phi_0)$. In the applications, one could use a coil coupled symmetrically to the loops instead of the individual couplings exploited here. It would then be possible to move along the direction $(0,0) \rightarrow (\Phi_0, \Phi_0)$ from the minimum to a position close to the maximum with just one rf control.

In Publication II we show that the critical current of the balanced SQUID agrees well with the zero-inductance model. To estimate the maximum suppression, we also consider the effect of the inductances. For this, it is convenient to express the equations of Sec. 3.2.2 in matrix form. The magnetic fluxes of the loops form the $n-1$ dimensional vector $\mathbf{\Phi}_{\mathrm{tot}} = \mathbf{\Phi}_{\mathrm{ext}} - \mathbf{L}\mathbf{I}$, where $\mathbf{\Phi}_{\mathrm{ext}} = (\Phi_1 \ldots \Phi_{n-1})^T$ are the external magnetic fluxes and $\mathbf{I} = (I_1 \ldots I_n)^T$ are currents through the individual junctions. The $(n-1) \times n$ inductance matrix $\mathbf{L}$ contains the coefficients L_{ji} which determine the magnetic flux induced to the loop j by the current I_i. Each inductance is a sum of geometric and kinetic parts. The geometric parts were calculated with FastHenry [114], and the kinetic parts from the resistivity and the physical size of the loops. We computed ϕ_i, calculated the resulting $\mathbf{\Phi}_{\mathrm{ext}}$ and $\mathbf{I}$, which were tabulated to find the maximum supercurrent corresponding to each $\mathbf{\Phi}_{\mathrm{ext}}$. One should note that some of these solutions may not be stable for small variations of the phases [115]. However, we neglected the stability considerations since their effect is expected to be small but numerically difficult to calculate in our case of low inductances, and because neglecting the stability considerations cannot give a too optimistic estimate for the suppression ratio of the critical current. A conservative estimate for the ratio was found to be > 300, which is an order of magnitude better than the typical suppression ratio for dc SQUIDs.

5.3 Potential of the Cooper pair sluice

Besides the Cooper pair sluice, only two other single-charge pumps we are aware of can generate nanoampere currents [33, 38]. Apart from the fact that the accuracy is still far too low for metrology, the device is interesting for other scientific purposes. For example, the sluice has been used for the experimental determination of the Berry phase [61, 107, 116].

Several ways to improve the accuracy have been proposed. The critical current suppression ratios of the balanced SQUID of Publication II might bring the sluice at least close to metrological accuracy [14]. Other alternatives are an array of sluices which could be operated with four rf control parameters [117]. Also operating two sluices in parallel in a superconducting loop could improve the

accuracy. These more sophisticated geometries are experimentally challenging, but they could benefit from the germanium process by which junctions with a smaller spread in their parameters can be fabricated.

Chapter 6

SINIS turnstile

The SINIS turnstile is based on the hybrid single-electron transistor, see Sec. 3.3. It was proposed originally in Ref. [15], where it was also realized in the NISIN configuration. However, already from the beginning it was expected that the SINIS turnstile would be more accurate. One reason is that in the NISIN structure, tunneling always heats the island, whereas in the SINIS case the island can be cooled, too. The NISIN turnstile may also suffer from unpredictable $1e/2e$ periodicity issues. In Ref. [15], the NISIN turnstile was $1e$ periodic. Furthermore, a detailed analysis of the higher-order tunneling processes shows that cotunneling limits the fundamental accuracy of the NISIN turnstile, whereas uncertainties below 10^{-8} are predicted for the SINIS version [86]. Hence we concentrate on the SINIS turnstile in this Thesis. The first experiments on the SINIS turnstile were reported in Publication III.

6.1 Operation of the turnstile

The operation of the turnstile is based on that the BCS gap expands the stability regions of the charge states, and the neighboring regions start to overlap, compare Figs. 3.2 and 3.6. The principle of operation of the turnstile is illustrated in Fig. 6.1. When the gate charge $n_{\mathrm{g}}(t)$ is alternated between two neighboring charge states, electrons are transported through the turnstile one by one. A small bias voltage, which yields a preferred direction of tunneling, can be applied since the current is ideally zero in the range $|eV_{\mathrm{b}}| < 2\Delta$ at any constant gate charge value. If the gate signal is extended to span $k+1$ charge states, one obtains current plateaus with k electrons pumped per cycle. However, the first plateau is optimal for metrology. Note that if a non-zero bias voltage is applied across a normal-state SET, a gate span between different charge states always passes a region where none of the charge states is stable and where the current can freely

flow through the device (white region in Fig. 6.1(a)). Hence the normal-state SET cannot act as a turnstile even in principle.

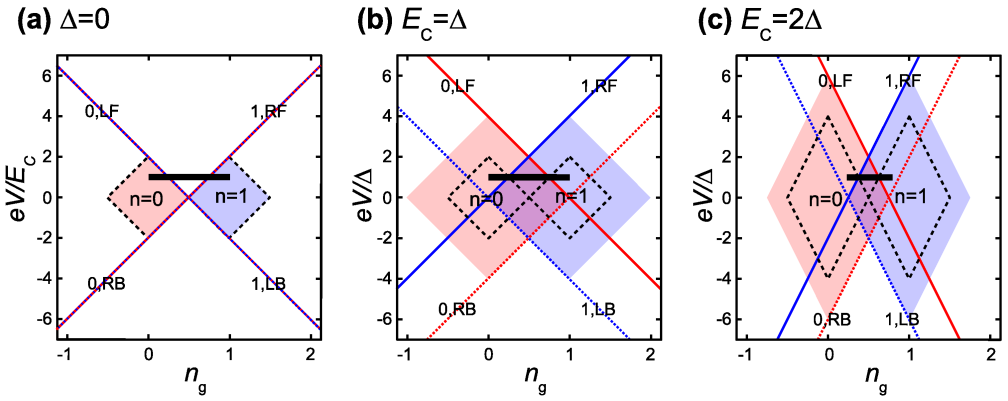

Figure 6.1: Schematic picture of pumping (a) with a normal SET, (b) with a hybrid SET with $E_c = \Delta$, and (c) with a hybrid SET with $E_c = 2\Delta$. The shaded areas are the stability regions of the charge states $n = 0$ and $n = 1$. The edges of the normal SET stability regions are drawn to all figures with dashed black lines. The long coloured lines represent the transition thresholds from states $n = 0$ and $n = 1$ by tunneling through the left (L) or the right (R) junction in the wanted forward (F, solid line) or unwanted backward (B, dashed line) direction. We define the bias voltage to be positive in the left electrode. Hence, the forward tunneling direction of electrons is from right to left. The thick black line corresponds to pumping with constant bias voltage $eV_b/\Delta = 1$ and a varying gate voltage [III].

A rough estimate for the optimal bias voltage based on thermal errors is presented in Ref. [15]. The probability of an electron tunneling in the wrong direction through the wrong junction is $\sim \exp(-eV_b/k_BT)$. This error, minimized by high bias, leads to no net charge transferred during the cycle. On the other hand, a too high bias increases the probability of transporting an extra electron which is $\sim \exp(-(2\Delta - eV_b)/k_BT)$. Combining these equations, we get $eV_b \approx \Delta$ as the optimum bias voltage, and a thermal error probability $\sim \exp(-\Delta/k_BT)$. The combined thermal error probability is $\ll 10^{-8}$ at realistic temperatures of about 100 mK and with the BCS gap of aluminum, $\Delta/k_B \approx 2.5$ K. Although the exact optimum of the bias can depend also on many other processes and a thorough study would be useful for the future, experimentally the choice $eV_b = \Delta$ seems optimal for most cases.

The gate drive is convenient to express as $n_g(t) = n_{g0} + A_g w(t)$ where n_{g0} and A_g are the gate offset and drive amplitude, respectively. The gate waveform, normalized to vary between ± 1, is denoted by $w(t)$. The optimal gate drive is symmetric with respect to the two charge states, hence the offset should be $n_{g0} =$

1/2. Here and in all pumping signal optimization discussion below we assume that $n_{g0} = 1/2$, which makes it possible to express the tunneling thresholds with the same amplitudes for both junctions. Based on the discussion above, we also assume that $eV_b = \Delta$. The optimal gate drive amplitude lies somewhere between the threshold amplitudes for forward and backward tunneling which are $A_{g,ft} = \Delta/4E_c$ and $A_{g,bt} = 3\Delta/4E_c$ for the optimum bias voltage, respectively. Experimentally, the sub-gap leakage appears to be strongest at the degeneracy point, but the forward tunneling rates are maximized at the extreme gate values. In this respect, a square-wave signal is optimal. On the other hand, passing the threshold for forward tunneling too quickly results into heating of the island, whereas a sine signal can also cool it, see Sec. 6.5. Hence, the optimal waveform may be of some intermediate form.

6.2 Theoretical limits

This section is mainly based on Ref. [86] which studies theoretically the fundamental limits of the turnstile based on higher-order tunneling processes. In that paper it is suggested to employ a square wave pumping signal. At zero temperature, the tunneling rate of Eq. (3.16) for a process with electrostatic energy change E_p becomes simply $\Gamma_p = \sqrt{E_p^2 - \Delta^2}/(R_{T,i}e^2)$. The tunneling rate depends on Δ, and since E_p is roughly proportional to $1/C_\Sigma$, the rate depends also on the $R_{T,i}C_\Sigma$ time constant, see Eq. (3.3). There are two chances per cycle to miss the transfer of one electron. The error rate of missed tunneling is simply $p_{miss} = 2\exp(-\Gamma_p/2f)$ for the square wave. The maximum pumping frequency by which the allowed error rate p_{miss} can be obtained is thus $f = \Gamma_p/[2\ln(2/p_{miss})]$.

As argued in Ref. [86], cotunneling is energetically forbidden in the SINIS turnstile, but it makes it impossible to reach metrological accuracy with the NISIN version. In the SINIS turnstile, the relevant higher-order processes are Andreev reflection (AR) and Cooper-pair–electron cotunneling (CPE). AR vanishes below the threshold amplitude $A_{g,AR} = 1/2 - \Delta/4E_c$. Together with the threshold $A_{g,ft}$, this yields the requirement $E_c > \Delta$ for pumping without AR induced errors. Then the limiting higher-order process is CPE, and it is theoretically possible to reach metrological accuracy.

In the CPE process, the transfer of a single electron over the whole transistor is correlated with the usual forward tunneling process. Hence, CPE transfers an extra electron, which is the opposite to the error of missed tunneling. Reference [86] sets both these error rates to the allowed error rate p and estimates the maximum current of the turnstile as a function of p. The maximum current increases rapidly as a function of E_c. However, the estimates are based on the amplitude $A_{g,AR}$, but in Publication IV we show that if $E_c > 2\Delta$, $A_{g,bt}$ sets

a more restrictive limit. Hence the maximum current with the error rate 10^{-8} saturates to somewhat above 10 pA estimated for $E_c = 3\Delta$. One should note that the analysis of the maximum current is based on the BCS gap of aluminum, $E_c/k_B \approx 2.5$ K. The maximum current could be increased by finding an alternative superconductor with a larger gap.

Parallelization of turnstiles is an attractive option because the structure and the operation of a single device is so simple [118]. Hence the theoretical result of 10 pA at 10^{-8} with a single turnstile is very promising. Experimentally, however, there are still unsolved problems. The most severe one appears to be the sub-gap leakage that was seen both in dc measurements and on the quantized current plateau in the first NISIN experiments [15]. The sub-gap leakage has not yet any conclusive theoretical description, and hence it was not included in the study of theoretical limits apart from the higher-order processes [86].

6.3 Sub-gap leakage of the SINIS turnstile

Publications III–VI report experimental results on the SINIS turnstile. Scanning electron micrographs of all types of studied samples are presented in Fig. 6.2. Publication III presents the first results on the SINIS turnstile. The importance of the charging energy [86] was not known prior to the sample fabrication, and hence we used the standard two-layer process. The sample with the charging energy of the order of $E_c/k_B \approx \Delta/k_B \approx 2.5$ K and Cu as the normal metal is presented in Fig. 6.2(a).

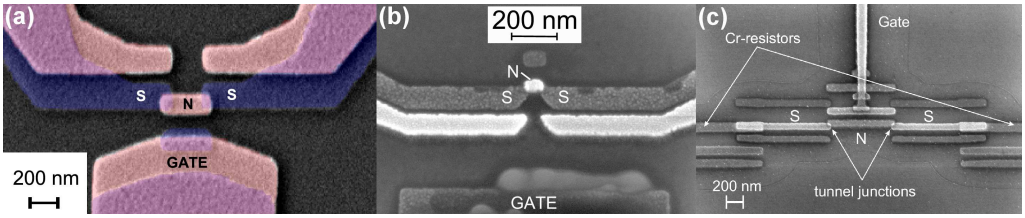

Figure 6.2: Scanning electron micrographs of (a) the first SINIS turnstile of Publication III, (b) the high-charging-energy turnstile of Publications IV–V, and (c) the turnstile in resistive environment of Publication VI [III, IV, VI].

The most important result of Publication III was the very small sub-gap leakage of $\eta < 10^{-5}$. In the first NISIN experiments, the leakage had been about $\eta \approx 10^{-4}$, i.e., of the same order of magnitude as in the SINIS structures without charging energy [15]. In Publication III, we also show a reduced slope on the quantized current plateau, in accordance with the expectation that it is related to the leakage. However, the plateaus become first rounded and then tilted as

the frequency is increased. The reason for this was heating coming from our deteriorated rf lines, which were upgraded before Publications IV-VI. The first NISIN results did not suffer severely from heating, which we think arises from the fact that the BCS gap makes the superconducting island less sensitive to temperature.

As mentioned in Sec. 3.3, the sub-gap leakage has usually been described with the smeared density of states (3.17). This Dynes model was originally suggested for taking into account the effect of the quasiparticle lifetime and Cooper pair breaking [75]. The density of states of Eq. (3.17) saturates to the value γ at low voltages, which produces the constant slope seen, e.g., in Fig. 3.6. However, the model is an approximation that was designed for the smearing of the gap edge, and not for describing the sub-gap states. Actually, it has been pointed out based on the microscopical theory of superconductors, that the Dynes model is possibly not the best approximation even for the gap edge [119]. The fact that the Dynes model fits well with the experiments should thus not be considered as a proof for the physical origin of the sub-gap leakage.

We did plenty of experiments to check that the low leakage of Publication III is reproducible. Since we do not yet understand the result completely, these data have not been published, but we report the present status here. First, we fabricated several sets of samples with two slightly different geometries and with two different normal metals, namely Cu and AuPd. We got some leaky samples, possibly due to pinholes, but in total, we measured 9 SINIS samples with a leakage below our measurement capabilities ($\eta < 10^{-5}$). Such samples were obtained with both geometries and materials. The tunnel barriers appeared to be more reproducible with AuPd, which we chose as the normal metal for Publications IV–V.

Measurement data of three AuPd samples with low leakage are presented in Fig. 6.3(a). To make the comparison between leakage ratios easier, the current is shown in the normalized form eIR_T/Δ_0, where $\Delta_0/e = 200$ μV is a typical BCS gap of aluminum. The parameters of the samples α, β and γ are $R_\mathrm{T} = 30$ kΩ and $E_\mathrm{c}/k_\mathrm{B} = 1.3$ K, $R_\mathrm{T} = 70$ kΩ and $E_\mathrm{c}/k_\mathrm{B} = 2.1$ K, and $R_\mathrm{T} = 90$ kΩ and $E_\mathrm{c}/k_\mathrm{B} = 2.5$ K, respectively. The leakage of all these samples seems to be at most $\eta \lesssim 1 \ldots 3 \times 10^{-6}$.

Since such low leakages have never been measured in large NIS junctions, we decided to study the effect of the junction size. We simplified the situation further by studying single NIS junctions. Results of two sets of NIS junctions (ABCD and abcde) are shown in Figs. 6.3(b–c). The area of the biggest junction was 0.03 μm^2 in both sets. Since all junctions of a set were metalized simultaneously, we can assume that the area resistivity is roughly constant within the set. Hence we can determine the size of the smaller junctions from the resistances. The leakage parameters are compared to the junction areas in Fig. 6.3(d).

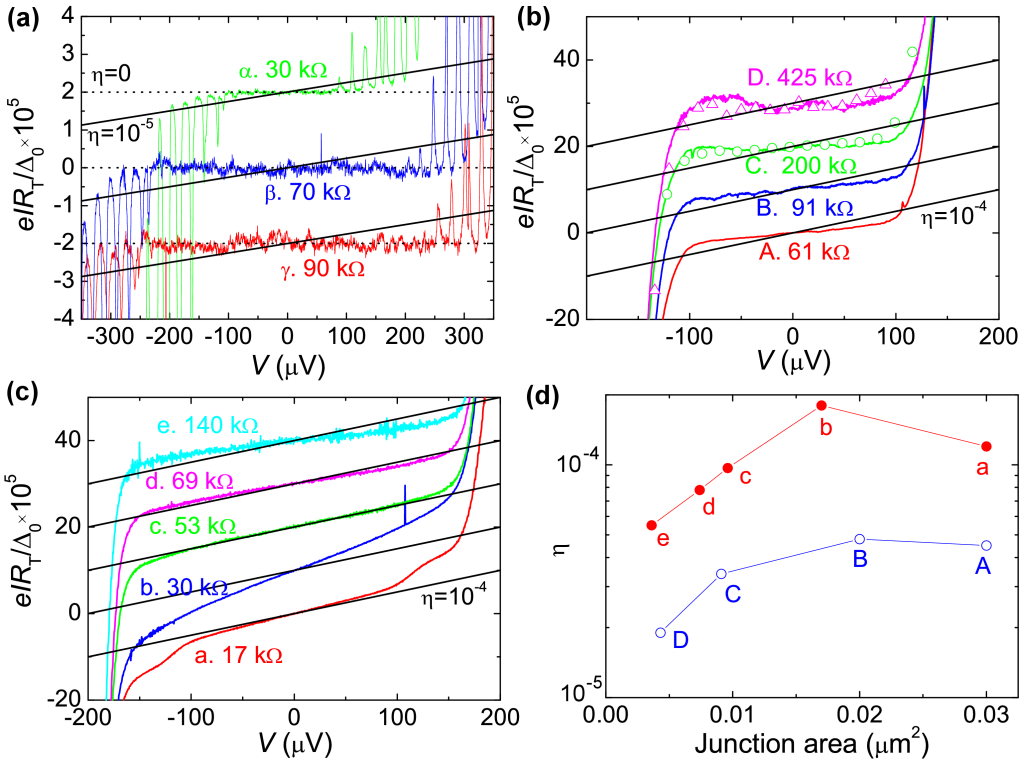

Figure 6.3: (a) Sub-gap IV curves of three AuPd SINIS samples with very low leakage. The gate voltage was swept during the measurement. Hence the envelopes correspond to gate-open and gate-closed states. (b) Sub-gap IV curves of NIS junction set ABCD. The leakages of the smallest junctions C and D were so low that they could not be determined with the routine measurements (lines). The circles and triangles show data averaged from tens of IV measurements. The data points of each IV measurement were taken in randomized order to prevent a slope due to a possible drift of the amplifier. (c) Sub-gap IV curves of the NIS junction set abcde. (d) Sub-gap leakages of the NIS junction sets ABCD and abcde as a function of the junction area.

Both NIS junction sets show decreasing leakage when the junction size is reduced. This indicates that the leakage may be related to Andreev reflection. Andreev reflection may depend on the junction size in two ways: (i) The Coulomb blockade can suppress the Andreev reflection [86, 89]. (ii) Andreev reflection may be enhanced by diffusive processes in large junctions [87, 89]. The first effect does not apply for single NIS junctions, but diffusive Andreev reflection may be the reason for the leakages of the order of $\eta \approx 10^{-4}$ in bigger junctions.

The next question is why are the leakages so much higher in set abcde than

in set ABCD? An obvious answer would be the difference in the area resistances, but we do not think that is correct. First, the low-leakage SINIS samples of Fig. 6.3(a) had also very low resistances. Second, after these measurements, such low leakages were no more observed, see Publication IV. We believe now that the reason for the increased leakage was that the rf lines of our cryostat were upgraded after the measurement of set ABCD. The new rf lines were designed for much higher gate drive frequencies than the old ones. Hence they may bring more noise to the samplestage, and cause photon-assisted leakage.

There are still several possible origins for the sub-gap leakage. For example, Andreev reflection, leakage due to nonequilibrium quasiparticles, and even ordinary single-electron tunneling may depend on the filtering of thermal noise [42]. Leakages in some individual samples can be caused by pinholes. We note that a magnetic field can smear the gap edge [120], but we checked experimentally (data not shown) that a magnetic field did not increase the leakage, which was originally of the magnitude $\eta \approx 10^{-4}$, even when the BCS gap was already significantly reduced by the field.

Some further insight to the sub-gap leakage issue is given by the experiments of Publication VI, where we studied the R-SINIS turnstile, i.e., the effect of on-chip CrO_x resistors with the sum resistance R_s on the turnstile, see Fig. 6.2(c). This recipe had been successfully used to improve the accuracy of the normal-state pump [28], where the resistors suppress cotunneling.

The main result of Publication VI is shown in Fig. 6.4. The leakage on the plateau in the pumping experiment was decreased by a factor 16 by the resistors. The question is, what is the reason for the improvement, as cotunneling is suppressed by the BCS gap even in the bare SINIS turnstile? The resistors are expected to suppress also Andreev reflection and Cooper-pair–electron cotunneling, but surprisingly, the improvement can be at least partially explained by first-order (single-electron) processes, see Fig. 6.4(b).

We modeled the single-electron tunneling rates in R-SINIS devices with the $P(E)$ formalism, see Sec. 3.4. The leakage was taken into account phenomenologically by the usual Dynes γ parameter. We found that the high-ohmic environment extends the plateau towards higher voltages, and decreases the slope. The maximum slope suppression ratio of about 17 was reached at the resistance $R_s = 100$ kΩ, which is well in accordance with the experiments. Interestingly, the minimum of the slope appears to be at the crossing point of $I = ef$. In these simulations, the high resistance decreases the effect of the intrinsic leakage of the junctions, whereas the previous measurements indicate that the electromagnetic environment might also cause the leakage in the limit of low but non-zero external impedance. One should note that the $P(E)$ distribution (3.22) is a narrow peak at low temperatures in the two opposite limits, i.e., when the external impedance is

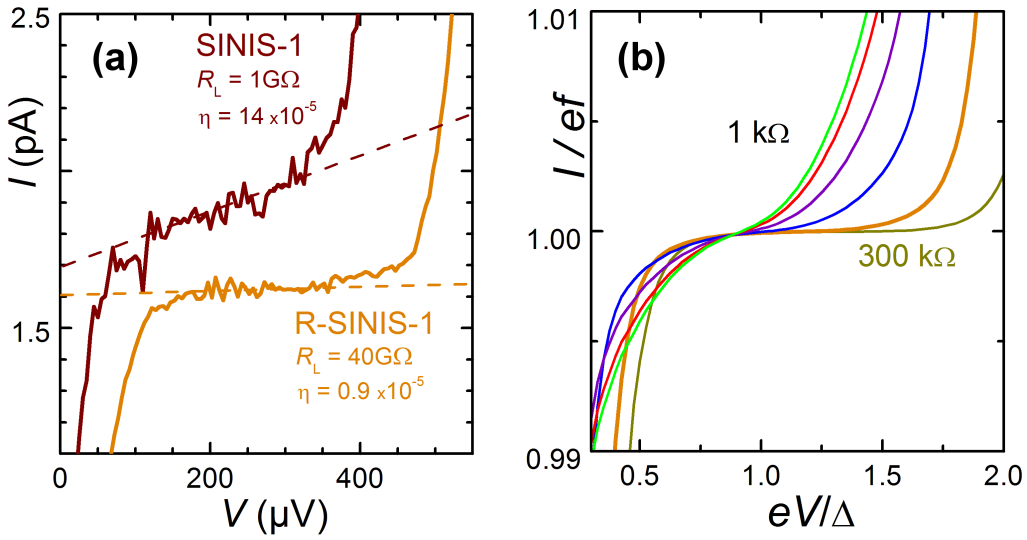

Figure 6.4: (a) Plateau of the R-SINIS turnstile at 10 MHz with $R_s \approx 80$ kΩ compared with a reference sample without resistors. The plateau of the bare SINIS sample is shifted by 0.3 pA for clarity. The symbol R_L implies the highest dynamic resistance along the plateau. (b) Pumping plateaus calculated for different resistances $R_s = 1, 3, 10, 30, 100, 300$ kΩ and fixed $R_T = 200$kΩ, $E_c = \Delta = 220$ μeV, $T = 100$ mK, $f = 10$ MHz, $n_{g0} = 0.5$, $A_g = 0.6$, and $\gamma = 10^{-4}$ [VI].

very low or very high. Between these extremes, the $P(E)$ distribution is broader, which may increase the leakage.

We simulated and measured the leakage at dc as well. The measured dc IV curves of both R-SINIS and bare SINIS samples show leakage that is negligible at low voltages, but rises nonlinearly and steeply above a threshold voltage. The leakage cannot be thus expressed with the simple parameter η. The resistive environment appears both to suppress the leakage and to increase the threshold. Similar results were obtained in measurements both at PTB and at TKK. Our simulations show qualitatively similar behaviour at higher resistances. At $R_s = 100$ kΩ, the sub-gap leakage is clearly nonlinear and suppressed. The island of both R-SINIS and bare SINIS samples was made out of Cr. The resistance of the island was thus significant, about 1–2 kΩ. This appears, however, not to be the reason for the nonlinearity of the leakage of the bare SINIS samples, since in this range, the simulated leakage is still almost linear and close to that of the usual model without resistances. The high leakage of the Al–Cr junctions at higher voltages is thus not completely described by our first-order model. One possible explanation is that a lower tunnel barrier quality increases Andreev re-

flection. Whatever the reason for the observed leakage is, it can be suppressed with the resistors. One should note, however, that at high frequencies, the resistors deteriorate the plateau due to the slow-down of tunneling and to the heating of the island.

6.4 Turnstile with high charging energy

In Publication IV, we study turnstile samples with charging energy of the order of $E_c \approx 3\Delta$, see Fig. 6.2(b). The resistances of the reported samples A, B and C were $R_T = 1540$ kΩ, 315 kΩ and 64 kΩ, respectively. While the other sample parameters were roughly identical, the large resistance variation made this set of samples ideal for studying the speed of the turnstile. A high pumping frequency is related to two kinds of errors: missed tunneling and backtunneling, i.e., tunneling in the direction against the bias. Missed tunneling could be seen as deviation from the linear increase of the current $I = ef$ as a function of frequency. However, this kind of a study would require a careful calibration of the rf line attenuation to keep the gate amplitude A_g applied to the sample constant. Also, deviations of the island temperature as a function of frequency might complicate the interpretation of the results. We found the backtunneling effect an easier way to compare experimental and theoretical tunneling rates.

Backtunneling can occur when the gate voltage is extended over the backtunneling thresholds, i.e., the dashed lines in Fig. 6.1(b–c). Tunneling in the forward direction is still preferred by the bias, but backtunneling can be statistically significant. With continuously rising waveforms like sine wave and at low frequencies, however, tunneling occurs typically before the backtunneling threshold is exceeded. This effect can be seen as backbending of the current plateaus in Fig. 6.5(a). Backbending was found relatively independent of the island temperature, and hence the slopes were nicely reproduced by our simulations based on the tunneling rates in Eq. (3.16). Fig. 6.5(a) demonstrates also that backtunneling is one reason why the first plateau is optimal for metrology.

In Fig. 6.5(b), we demonstrate the highest currents achieved with the SINIS turnstile so far. Even the second plateau of sample C is relatively flat at 500 MHz. The backtunneling effect is much weaker than in Fig. 6.5(a) mainly because the resistance of the sample is much lower and partly because of a higher bias voltage. However, this experiment could not be captured accurately by our constant-temperature simulations, since there is already significant temperature-induced leakage at the highest plateaus. More ideal behaviour is expected at the same current level at the first plateau. However, we were limited by the maximum frequency of our rf generator, which is 500 MHz.

In Fig. 6.6(a), we show the effect of backtunneling on the first plateau. Above

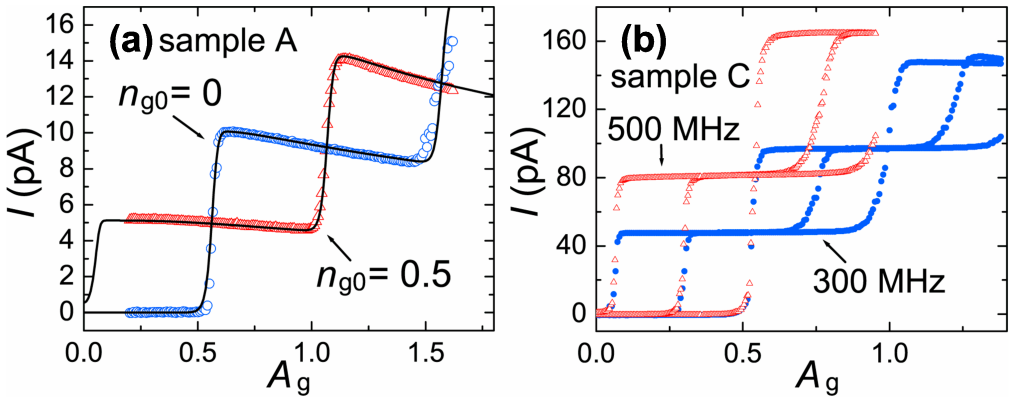

Figure 6.5: (a) Current of sample A vs gate amplitude with 32 MHz sine wave and at $eV_b = 0.8\Delta$. The lines show the corresponding simulated currents. (b) Measured plateaus of sample C with 300 MHz and 500 MHz sinusoidal drives and at $n_{g0} = 0, 0.25$ and 0.5. The bias voltage was $eV_b = 1.36\Delta$ [IV].

the backtunneling threshold $A_{g,bt}$, the current depends clearly on the drive frequency. Since $A_{g,bt}$ is inversely proportional to the charging energy, pumping with high charging energies is limited to relatively low amplitudes, which limits the maximum current of turnstiles with $E_c > 2\Delta$. Also the plateau as a function of A_g becomes narrower, which sets requirements for the noise of the gate signal, but does not appear to limit the operation of the turnstile yet at $E_c \approx 3\Delta$.

In Fig. 6.6(b), we demonstrate that passing the degeneracy point quickly with a square wave suppresses the effect of the sub-gap leakage. The plateau with the square wave is clearly flatter and wider than with the sine wave. We note also, that the measurements of Fig. 6.6 are traceable to the national low-current standard of MIKES, see Sec. 4.3. We show thus that the magnitude of the quantized current is correct at about 10 pA with the uncertainty of about 10^{-3}.

6.5 Radio frequency refrigeration

In Publication V, our focus is not on pumping charge, but on pumping heat. As discussed in Sec. 3.3, dc biased SINIS structures are routinely used as microcoolers. The motivation for local electronic cooling arises from the development of nanodevices. Light-weight and energy saving coolers could be useful, e.g., for the noise reduction of spaceborne sensors [70]. Sometimes the SINIS structure cannot be biased optimally for cooling, which is the case, e.g., for the turnstile where the dc cooling effect is insignificant at the optimal operation conditions,

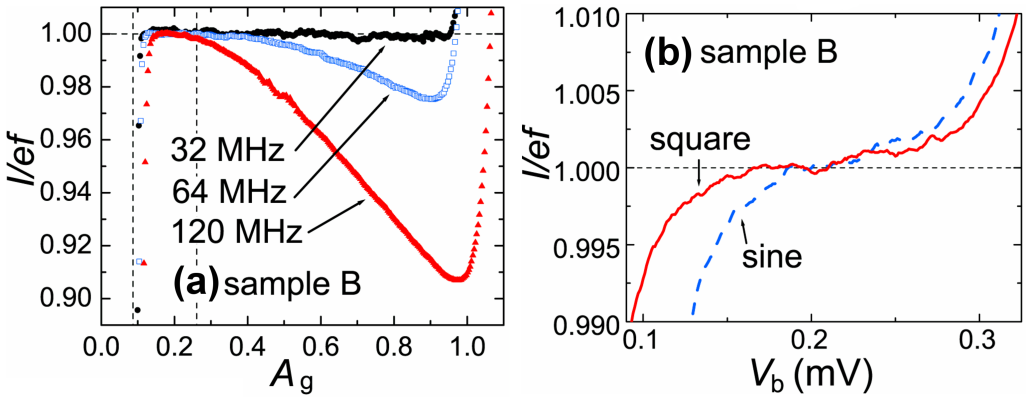

Figure 6.6: (a) First plateau of sample B at sine wave. The frequencies are 120 MHz, 64 MHz, and 32 MHz. $A_{\mathrm{g,ft}}$ and $A_{\mathrm{g,bt}}$ are marked with the dashed vertical lines. (b) First plateau of sample B as a function of bias voltage at 64 MHz at sine wave and square wave [IV].

i.e., $T_{\mathrm{bath}} < 100$ mK and $eV_{\mathrm{b}} = \Delta$. In such cases, cooling can be achieved by cyclic radio frequency refrigeration, as suggested in Ref. [71] and discussed further in Ref. [121]. The rf cooling method is particularly useful for Coulomb blockaded devices where the electronic temperature of the island can otherwise be higher than that of the cryostat. Gate-controlled refrigeration was demonstrated at dc in the so-called heat transistor [72], but the rf refrigeration method had not been proven due to difficulties in thermometry before Publication V.

The principle of rf refrigeration in the turnstile is illustrated in Fig. 6.7. We do not use any external thermometer, but we determine the temperature from the charge current of the turnstile. A method resembling ours has been used before for ordinary dc cooling [122]. In the optimal turnstile operation, the charge current should be insensitive to any experimental details including temperature. Hence we have to drive the turnstile far from the optimal conditions to be able to extract information out of the charge current. In practice, we increased the bath temperature to about 200–300 mK. Cooling does not require any bias voltage, but we used a bias voltage of 50 μV ($\approx 0.25\Delta/e$) which is high enough for determining the temperature of the island, but low enough to avoid dc cooling, see Fig. 3.6(d).

For the demonstration of the cooling effect, we used the same sample as in Publication IV (sample B). We used the zero-bias leakage resistance of the sample to determine the bath temperature. Sub-gap IV curves at bath temperatures between about 180 mK and 415 mK were used to fit the electron-phonon coupling constant of AuPd. Below about 350 mK, the best fit was given by $\Sigma \approx 4 \times 10^9$ W/m^{3}K^5, which is in accordance with Ref. [123]. At about 400 mK the best fit was given by $\Sigma \approx 3.5 \times 10^9$ W/m^{3}K^5, which may be an indication of phonon

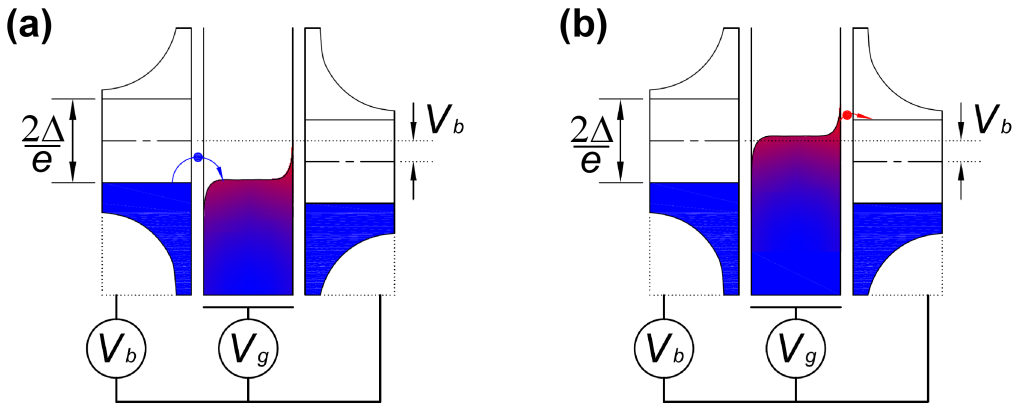

Figure 6.7: Principle of rf refrigeration in the turnstile. Current and thus cooling is blocked at any dc gate value. When the potential of the island is ramped down (a), tunneling to the island becomes first possible for the lowest-energy empty states. When the potential of the island is ramped up (b), tunneling out from the island becomes first possible for the highest energy states. Due to the Coulomb blockade, only a single electron can tunnel through the device during one cycle [V].

cooling [122]. Hence the value fitted for the lower temperatures is the correct one.

In Fig. 6.8, we show the effect of rf refrigeration on the rise to the first quantized current plateau. Due to the high temperature and the low bias voltage, the turnstile never reaches the plateau. We compare the measured I vs A_g curve to two simulated curves. Both are based on the orthodox model and the sample parameters extracted from the dc measurements. We take some initial probability distribution of charge states, and start to simulate the time development of the charge distribution under varying $n_\mathrm{g}(t)$. Usually already after the first gate cycle, the charge distribution does not any more depend on the initial distribution, but only on the phase of the gate cycle. Then we integrate the total heat and charge transferred during the second gate cycle. We compare the heat transfer of tunneling to that of the electron–phonon coupling, and search iteratively for an island temperature that yields zero net heat transfer. As the result of the iteration, we find both simulated temperature and charge current. For comparison, we simulated the current also in the case that the island stays at the bath temperature. The simulated cooling effect is maximized when the gate amplitude is at $A_\mathrm{g,ft}$. Close to this value, there is also the strongest deviation between the charge currents in the two types of simulations. The simulation that includes the cooling effect gives an excellent fit to the experiment. It seems that the cooling effect creates a charge current peak that tries to reach the quantized plateau.

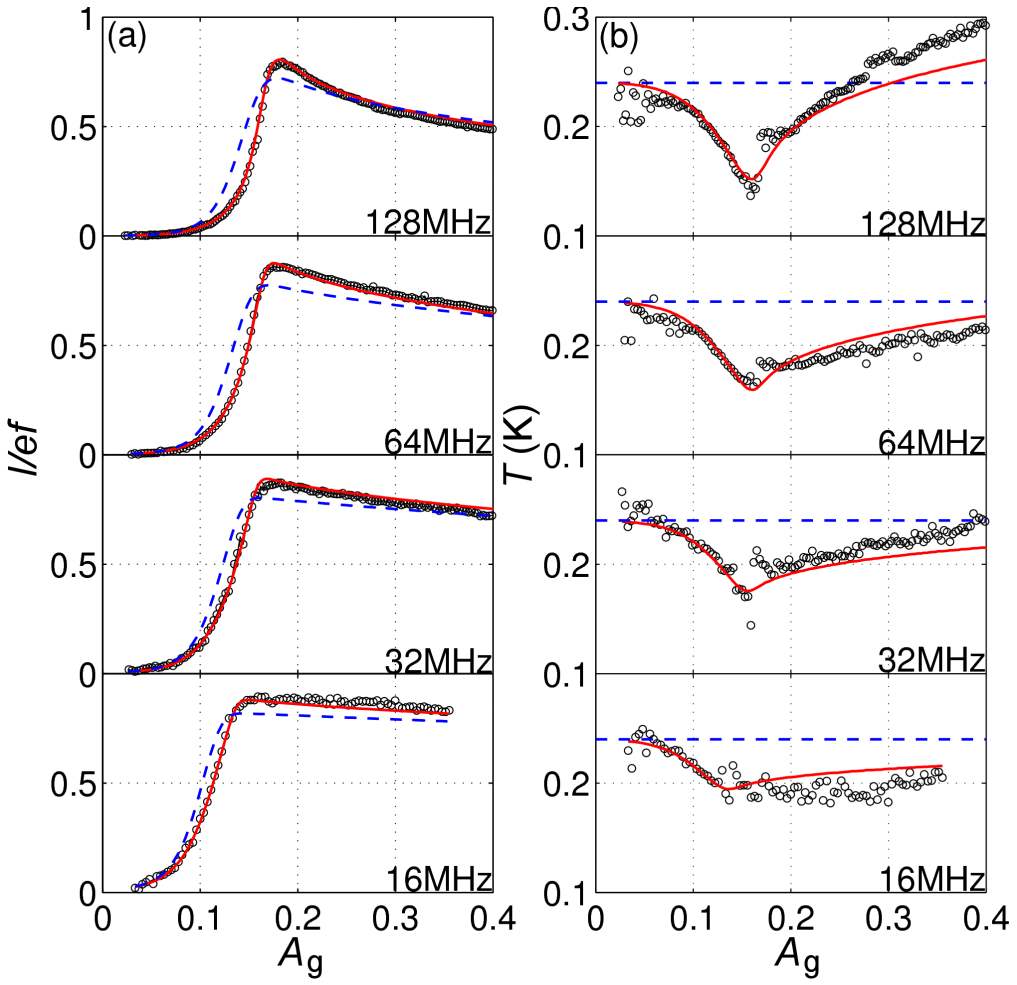

Figure 6.8: (a) Current of the turnstile as a function of A_g at $T_{bath} = 240$ mK, $V_b = 50$ μV, and $n_{g0} \approx 0.5$. Simulations taking into account the cooling effect are shown by the red lines. Simulations assuming that the island stays at T_{bath} are shown by the blue lines. (b) Red lines show the simulated island temperature. The circles show the island temperature extracted from the current measurement with the help of the simulation [V].

We should note that we used a single fitting parameter in the simulation, namely n_{g0}. The best fit was given by $n_{g0} \approx 0.48 \ldots 0.49$ instead of the experimentally set value $n_{g0} = 0.5$. We think the reason for this is that the experimental curve was smeared by background charge fluctuations.

In Fig. 6.8(b), we compare the simulated temperature to temperature extracted from the current measurement with the help of a simulation. For the

extracted temperature, we searched iteratively for an island temperature that reproduces the measured current. There is a good agreement between the simulated and the extracted temperatures, although the temperature extraction process is very sensitive to any experimental nonidealities like smearing.

In Publication V, we also show that the cooling power is proportional to the pumping frequency up to the saturation frequency of about 100 MHz arising from the finite tunneling rates. The single-electron turnstile works thus not only as a charge (ef) pump, but also as a heat ($k_{\mathrm{B}}Tf$) pump [71]. Demonstration of the rf cooling effect is interesting itself, but it is also essential for the turnstile, although in that case it is not important really to cool the island, but merely not to heat it. We found an excellent fit between measurements and simulations under many different experimental conditions, which shows that the properties of the turnstile can be described with the orthodox theory on the present level.

6.6 Overview of the turnstile

In Publications III-VI, we progressed from the first demonstration of turnstile operation in the SINIS structure to studies of the physics behind the turnstile. We have studied turnstiles with high charging energy and turnstiles in resistive environment. It seems that the physics of the turnstile is well understood with the exception of the sub-gap leakage. The results of Publications III and VI indicate though, that this leakage issue can be solved. The BCS gap of aluminum limits the theoretical maximum current of the present turnstiles to about 10 pA at metrological accuracy. However, the current level required for the quantum metrological triangle (> 100 pA) could be reached by the parallelization of turnstiles, which is a tempting option due to the simplicity of the operation of a single device [118].

Chapter 7

Conclusions

In this Thesis, two candidates for a quantum current standard are studied: the Cooper pair sluice and the SINIS turnstile. To date, quantum standards have been limited to current magnitudes of the order of 1 pA [11]. However, current in the range of 100 pA–1 nA would be required for practical metrological applications and for closing the quantum metrological triangle. The latter could have an impact on changing the SI system of units to be based on fundamental constants.

There are several candidate devices for a current standard in the sub-nA range. As shown in Publication I, the Cooper pair sluice is one of the very few single-charge devices that can generate currents above 1 nA [33, 38]. However, improving its relative accuracy to the metrologically interesting range $\ll 10^{-6}$ is very difficult.

The SINIS turnstile seems more promising for metrological purposes. In Publication IV, after only two years from the original idea [15], we demonstrated an accuracy of the order of 10^{-3} which was already so good that it was difficult to determine with conventional non-quantum low-current devices. We also demonstrated a relatively flat plateau at as high current as 160 pA, although we must note that the metrological operation of the device is limited to about 10 pA even in theory [86]. However, the operation of the turnstile requires only a single rf control parameter, which makes parallelization a promising way to increase the current to the 100 pA level [118]. Of the many novel candidates for a current standard, only the SINIS turnstile and two types of semiconducting pumps [34, 38] are being actively developed towards metrological accuracy at the moment.

The development of metrological standards is also related to other scientific progress. In Publication II, we demonstrate the balanced SQUID, a new type of SQUID structure, which can be used to turn Josephson coupling on and off with a high ratio in many kinds of applications including the Cooper pair sluice. The Cooper pair sluice can be used also for the experimental determination of the

Berry phase [61]. In Publications III and VI we demonstrate that the sub-gap leakage ratio of SINIS structures can be lowered significantly below the typical value $\eta \approx 10^{-4}$. This is crucial not only for the turnstile, but also for the development of solid-state microcoolers. Furthermore, in Publication V we show that the hybrid single-electron transistor can be used also as a novel type of microcooler, a single-electronic radio frequency refrigerator.

Bibliography

[1] Bureau International des Poids et Mesures, *The International System of Units (SI)*, 8 ed. (STEDI Media, Paris, 2006).

[2] J. C. Maxwell, Address to the Mathematical and Physical Sections of the British Association, Liverpool, 1870.

[3] J. Flowers, Science **306**, 1324 (2004).

[4] B. D. Josephson, Phys. Lett. **1**, 251 (1962).

[5] K. von Klitzing, G. Dorda, and M. Pepper, Phys. Rev. Lett. **45**, 494 (1980).

[6] D. V. Averin and K. K. Likharev, J. Low Temp. Phys. **62**, 345 (1986).

[7] D. V. Averin and K. K. Likharev, Mesoscopic Phenomena in Solids, 1991.

[8] K. K. Likharev and A. B. Zorin, J. Low Temp. Phys. **59**, 347 (1985).

[9] L. J. Geerligs, V. F. Anderegg, P. A. M. Holweg, J. E. Mooij, H. Pothier, D. Esteve, C. Urbina, and M. H. Devoret, Phys. Rev. Lett. **64**, 2691 (1990).

[10] H. Pothier, P. Lafarge, C. Urbina, D. Esteve, and M. H. Devoret, Europhys. Lett. **17**, 249 (1992).

[11] M. W. Keller, J. M. Martinis, N. M. Zimmerman, and A. H. Steinbach, Appl. Phys. Lett. **69**, 1804 (1996).

[12] M. W. Keller, A. L. Eichenberger, J. M. Martinis, and N. M. Zimmerman, Science **285**, 1706 (1999).

[13] J. Gallop, Phil. Trans. Royal Soc. A **363**, 2221 (2005).

[14] A. O. Niskanen, J. P. Pekola, and H. Seppä, Phys. Rev. Lett. **91**, 177003 (2003).

[15] J. P. Pekola, J. J. Vartiainen, M. Möttönen, O.-P. Saira, M. Meschke, and D. V. Averin, Nature Phys. **4**, 120 (2008).

[16] W. K. Clothier, G. J. Sloggett, H. Bairnsfather, M. F. Currey, and D. J. Benjamin, Metrologia **26**, 9 (1989).

[17] A. Eichenberger, B. Jeckelmann, and P. Richard, Metrologia **40**, 356 (2003).

[18] R. L. Steiner, E. R. Williams, D. B. Newell, and R. Liu, Metrologia **42**, 431 (2005).

[19] P. Becker, Metrologia **40**, 366 (2003).

[20] I. M. Mills, P. J. Mohr, T. J. Quinn, B. N. Taylor, and E. R. Williams, Metrologia **42**, 71 (2005).

[21] I. M. Mills, P. J. Mohr, T. J. Quinn, B. N. Taylor, and E. R. Williams, Metrologia **43**, 227 (2006).

[22] P. Becker, P. D. Bievre, K. Fujii, M. Glaeser, B. Inglis, H. Luebbig, and G. Mana, Metrologia **44**, 1 (2007).

[23] M. J. T. Milton, J. M. Williams, and S. J. Bennett, Metrologia **44**, 356 (2007).

[24] M. W. Keller, Metrologia **45**, 102 (2008).

[25] M. W. Keller, N. M. Zimmerman, and A. L. Eichenberger, Metrologia **44**, 505 (2007).

[26] A. M. Thompson and D. G. Lampard, Nature **177**, 888 (1956).

[27] N. Feltin and F. Piquemal, Eur. Phys. J. Spec. Top. **172**, 267 (2009).

[28] S. V. Lotkhov, S. A. Bogoslovsky, A. B. Zorin, and J. Niemeyer, Appl. Phys. Lett. **78**, 946 (2001).

[29] B. Steck, A. Gonzalez-Cano, N. Feltin, L. Devoille, F. Piquemal, S. Lotkhov, and A. B. Zorin, Metrologia **45**, 482 (2008).

[30] L. J. Geerligs *et al.*, Zeitschrift für Physik B Condensed Matter **85**, 349 (1991).

[31] J. E. Mooij and Y. V. Nazarov, Nature Phys. **2**, 169 (2006).

[32] F. Nguyen, N. Boulant, G. Ithier, P. Bertet, H. Pothier, D. Vion, and D. Esteve, Phys. Rev. Lett. **99**, 187005 (2007).

[33] J. M. Shilton, V. I. Talyanskii, M. Pepper, D. A. Ritchie, J. E. F. Frost, C. J. B. Ford, C. G. Smith, and G. A. C. Jones, J. Phys. Condens. Matter **8**, L531 (1996).

[34] M. D. Blumenthal *et al.*, Nature Phys. **3**, 343 (2007).

[35] S. J. Wright *et al.*, Phys. Rev. B **78**, 233311 (2008).

[36] B. Kaestner, C. Leicht, V. Kashcheyevs, K. Pierz, U. Siegner, and H. W. Schumacher, Appl. Phys. Lett. **94**, 012106 (2009).

[37] A. Fujiwara, N. M. Zimmerman, Y. Ono, and Y. Takahashi, Appl. Phys. Lett. **84**, 1323 (2004).

[38] A. Fujiwara, K. Nishiguchi, and Y. Ono, Appl. Phys. Lett. **92**, 042102 (2008).

[39] J. Bylander, T. Duty, and P. Delsing, Nature **434**, 361 (2005).

[40] M. Wulf and A. B. Zorin, arXiv:0811.3927 (2008).

[41] M. H. Devoret, D. Esteve, and C. Urbina, Nature **360**, 547 (1992).

[42] G. L. Ingold and Y. V. Nazarov, in *Single charge tunneling*, Vol. 294 of *NATO ASI Series B*, edited by H. Grabert and M. H. Devoret (Plenum Press, New York, 1992), pp. 21–107.

[43] G. Schön, in *Quantum transport and dissipation*, edited by T. Dittrich, P. Hänggi, G.-L. Ingold, B. Kramer, G. Schön, and W. Zwerger (Wiley-VCH, Berlin, 1998), Chap. 3.

[44] K. Likharev, Proceedings of the IEEE **87**, 606 (1999).

[45] H. Pothier, S. Guéron, N. O. Birge, D. Esteve, and M. H. Devoret, Phys. Rev. Lett. **79**, 3490 (1997).

[46] M. Tinkham, *Introduction to superconductivity*, 2 ed. (McGraw-Hill, New York, 1996).

[47] J. Aumentado, M. W. Keller, J. M. Martinis, and M. H. Devoret, Phys. Rev. Lett. **92**, 066802 (2004).

[48] S. Corlevi, W. Guichard, F. W. J. Hekking, and D. B. Haviland, Phys. Rev. B **74**, 224505 (2006).

[49] A. J. Ferguson, N. A. Court, F. E. Hudson, and R. G. Clark, Phys. Rev. Lett. **97**, 106603 (2006).

[50] T. Yamamoto, Y. Nakamura, Y. A. Pashkin, O. Astafiev, and J. S. Tsai, Appl. Phys. Lett. **88**, 212509 (2006).

[51] A. M. Savin, M. Meschke, J. P. Pekola, Y. A. Pashkin, T. F. Li, H. Im, and J. S. Tsai, Appl. Phys. Lett. **91**, 063512 (2007).

[52] S. J. MacLeod, S. Kafanov, and J. P. Pekola, Appl. Phys. Lett. **95**, 052503 (2009).

[53] K. K. Likharev, *Dynamics of Josephson junctions and circuits* (Gordon and Breach Science, Amsterdam, 1986).

[54] T. Van Duzer and C. W. Turner, *Principles of superconductive devices and circuits*, 2 ed. (Prentice Hall, New Jersey, 1998).

[55] V. Ambegaokar and A. Baratoff, Phys. Rev. Lett. **10**, 486 (1963).

[56] J. M. Kivioja, T. E. Nieminen, J. Claudon, O. Buisson, F. W. J. Hekking, and J. P. Pekola, Phys. Rev. Lett. **94**, 247002 (2005).

[57] J. M. Kivioja, T. E. Nieminen, J. Claudon, O. Buisson, F. W. J. Hekking, and J. P. Pekola, New J. Phys. **7**, 179 (2005).

[58] V. M. Krasnov, T. Bauch, S. Intiso, E. Hurfeld, T. Akazaki, H. Takayanagi, and P. Delsing, Phys. Rev. Lett. **95**, 157002 (2005).

[59] J. Männik, S. Li, W. Qiu, W. Chen, V. Patel, S. Han, and J. E. Lukens, Phys. Rev. B **71**, 220509 (2005).

[60] D. Vion, A. Aassime, A. Cottet, P. Joyez, H. Pothier, C. Urbina, D. Esteve, and M. H. Devoret, Science **296**, 886 (2002).

[61] M. Möttönen, J. J. Vartiainen, and J. P. Pekola, Phys. Rev. Lett. **100**, 177201 (2008).

[62] Y. Nakamura, Y. A. Pashkin, and J. S. Tsai, Nature **398**, 786 (1999).

[63] Y. Makhlin, G. Schön, and A. Shnirman, Rev. Mod. Phys. **73**, 357 (2001).

[64] M. Nahum, T. M. Eiles, and J. M. Martinis, Appl. Phys. Lett. **65**, 3123 (1994).

[65] M. M. Leivo, J. P. Pekola, and D. V. Averin, Appl. Phys. Lett. **68**, 1996 (1996).

[66] A. M. Clark *et al.*, Appl. Phys. Lett. **86**, 173508 (2005).

[67] M. Nahum and J. M. Martinis, Appl. Phys. Lett. **63**, 3075 (1993).

[68] D. R. Schmidt, C. S. Yung, and A. N. Cleland, Appl. Phys. Lett. **83**, 1002 (2003).

[69] M. Meschke, W. Guichard, and J. P. Pekola, Nature **444**, 187 (2006).

[70] F. Giazotto, T. T. Heikkilä, A. Luukanen, A. M. Savin, and J. P. Pekola, Rev. Mod. Phys. **78**, 217 (2006).

[71] J. P. Pekola, F. Giazotto, and O.-P. Saira, Phys. Rev. Lett. **98**, 037201 (2007).

[72] O.-P. Saira, M. Meschke, F. Giazotto, A. M. Savin, M. Möttönen, and J. P. Pekola, Phys. Rev. Lett. **99**, 027203 (2007).

[73] P. Koppinen, T. Kühn, and I. Maasilta, J. Low Temp. Phys. **154**, 179 (2009).

[74] J. P. Pekola, T. T. Heikkilä, A. M. Savin, J. T. Flyktman, F. Giazotto, and F. W. J. Hekking, Phys. Rev. Lett. **92**, 056804 (2004).

[75] R. C. Dynes, J. P. Garno, G. B. Hertel, and T. P. Orlando, Phys. Rev. Lett. **53**, 2437 (1984).

[76] J. Jochum *et al.*, J. Appl. Phys. **83**, 3217 (1998).

[77] J. P. Pekola, D. V. Anghel, T. I. Suppula, J. K. Suoknuuti, A. J. Manninen, and M. Manninen, Appl. Phys. Lett. **76**, 2782 (2000).

[78] A. V. Timofeev, C. P. Garcia, N. B. Kopnin, A. M. Savin, M. Meschke, F. Giazotto, and J. P. Pekola, Phys. Rev. Lett. **102**, 017003 (2009).

[79] A. O. Caldeira and A. J. Leggett, Annals of Physics **149**, 374 (1983).

[80] G.-L. Ingold, H. Grabert, and U. Eberhardt, Phys. Rev. B **50**, 395 (1994).

[81] T. Holst, D. Esteve, C. Urbina, and M. H. Devoret, Phys. Rev. Lett. **73**, 3455 (1994).

[82] A. Steinbach, P. Joyez, A. Cottet, D. Esteve, M. H. Devoret, M. E. Huber, and J. M. Martinis, Phys. Rev. Lett. **87**, 137003 (2001).

[83] Y. M. Ivanchenko and L. A. Zil'berman, Sov. Phys. JETP **28**, 1272 (1969).

[84] D. V. Averin and Y. V. Nazarov, in *Single charge tunneling*, Vol. 294 of *NATO ASI Series B*, edited by H. Grabert and M. H. Devoret (Plenum Press, New York, 1992).

[85] S. V. Lotkhov, S. A. Bogoslovsky, A. B. Zorin, and J. Niemeyer, Phys. Rev. Lett. **91**, 197002 (2003).

[86] D. V. Averin and J. P. Pekola, Phys. Rev. Lett. **101**, 066801 (2008).

[87] S. Rajauria, P. Gandit, T. Fournier, F. W. J. Hekking, B. Pannetier, and H. Courtois, Phys. Rev. Lett. **100**, 207002 (2008).

[88] T. M. Eiles, J. M. Martinis, and M. H. Devoret, Phys. Rev. Lett. **70**, 1862 (1993).

[89] J. M. Hergenrother, M. T. Tuominen, and M. Tinkham, Phys. Rev. Lett. **72**, 1742 (1994).

[90] G. J. Dolan, Appl. Phys. Lett. **31**, 337 (1977).

[91] R. Howard, E. Hu, and L. Jackel, IEEE Trans. Electr. Dev. **28**, 1378 (1981).

[92] Y. A. Pashkin, Y. Nakamura, and J. S. Tsai, Appl. Phys. Lett. **76**, 2256 (2000).

[93] J. Pekola and J. Kauppinen, Cryogenics **34**, 843 (1994).

[94] J. M. Martinis and M. Nahum, Phys. Rev. B **48**, 18316 (1993).

[95] J. M. Martinis, M. H. Devoret, and J. Clarke, Phys. Rev. B **35**, 4682 (1987).

[96] A. Lukashenko and A. V. Ustinov, Rev. Sci. Instrum. **79**, 014701 (2008).

[97] H. le Sueur and P. Joyez, Rev. Sci. Instrum. **77**, 115102 (2006).

[98] A. B. Zorin, Rev. Sci. Instrum. **66**, 4296 (1995).

[99] K. Bladh *et al.*, Rev. Sci. Instrum. **74**, 1323 (2003).

[100] K. Schwab, E. A. Henriksen, J. M. Worlock, and M. L. Roukes, Nature **404**, 974 (2000).

[101] G.-D. Willenberg, H. Tauscher, and P. Warnecke, IEEE Trans. Instrum. Meas. **52**, 436 (2003).

[102] H. van den Brom, P. de la Court, and G. Rietveld, IEEE Trans. Instrum. Meas. **54**, 554 (2005).

[103] N. E. Fletcher, S. P. Giblin, J. M. Williams, and K. J. Lines, IEEE Trans. Instrum. Meas. **56**, 326 (2007).

[104] I. Iisakka, K. Kalliomäki, J. Seppälä, and A. Manninen, in *Conference on Precision Electromagnetic Measurements Digest*, edited by A. H. Cookson (Johnson Printing, USA, 2008), p. 352.

[105] G. Rietveld and H. van den Brom, IEEE Trans. Instrum. Meas. **56**, 559 (2007).

[106] J. P. Pekola, J. J. Toppari, M. Aunola, M. T. Savolainen, and D. V. Averin, Phys. Rev. B **60**, R9931 (1999).

[107] M. Möttönen, J. P. Pekola, J. J. Vartiainen, V. Brosco, and F. W. J. Hekking, Phys. Rev. B **73**, 214523 (2006).

[108] A. O. Niskanen, J. M. Kivioja, H. Seppä, and J. P. Pekola, Phys. Rev. B **71**, 012513 (2005).

[109] S. V. Lotkhov, S. A. Bogoslovsky, A. B. Zorin, and J. Niemeyer, J. Appl. Phys. **95**, 6325 (2004).

[110] L. Faoro, J. Siewert, and R. Fazio, Phys. Rev. Lett. **90**, 028301 (2003).

[111] M. Cholascinski, Phys. Rev. B **69**, 134516 (2004).

[112] M. Cholascinski, Phys. Rev. Lett. **94**, 067004 (2005).

[113] F. Chiarello *et al.*, Appl. Phys. Lett. **93**, 042504 (2008).

[114] See `http://www.fastfieldsolvers.com`.

[115] C. Lucheroni, Phys. Rev. B **55**, 6559 (1997).

[116] M. Aunola and J. J. Toppari, Phys. Rev. B **68**, 020502 (2003).

[117] M. Cholascinski and R. W. Chhajlany, Phys. Rev. Lett. **98**, 127001 (2007).

[118] V. F. Maisi, Y. A. Pashkin, S. Kafanov, J. S. Tsai, and J. P. Pekola, arXiv:0908.2357 (2009).

[119] B. Mitrovic and L. A. Rozema, J. Phys. Cond. Matt. **20**, 015215 (2008).

[120] A. Anthore, H. Pothier, and D. Esteve, Phys. Rev. Lett. **90**, 127001 (2003).

[121] N. B. Kopnin, F. Taddei, J. P. Pekola, and F. Giazotto, Phys. Rev. B **77**, 104517 (2008).

[122] S. Rajauria, P. S. Luo, T. Fournier, F. W. J. Hekking, H. Courtois, and B. Pannetier, Phys. Rev. Lett. **99**, 047004 (2007).

[123] A. V. Timofeev, M. Helle, M. Meschke, M. Möttönen, and J. P. Pekola, Phys. Rev. Lett. **102**, 200801 (2009).